The *Drosophila* chemokine-like Orion bridges phosphatidylserine and Draper in phagocytosis of neurons

Hui Ji[1], Bei Wang[1], David Labib[1,3], Joyce Lei[1,4], Xinchen Chen[1], Maria Sapar[1,3], Ana Boulanger[2], Jean-Maurice Dura[2] and Chun Han[1,*]

[1]Weill Institute for Cell and Molecular Biology and Department of Molecular Biology and Genetics, Cornell University, Ithaca, NY 14853, USA

[2]IGH, Univ Montpellier, CNRS, Montpellier, France

[3]Current address: The New York Stem Cell Foundation Research Institute, New York, NY 10019, USA

[4]Current address: Tisch MS Research Center of New York, New York, NY 10019, USA

[*]Correspondence: chun.han@cornell.edu

RUNNING TITLE

Orion bridges PS and Drpr in neuronal phagocytosis

SUMMARY

Phagocytic clearance of degenerating neurons is mediated by "eat-me" signals exposed on the neuronal surface. The conserved neuronal eat-me signal phosphatidylserine (PS) is detected by resident phagocytes through specialized recognition systems. The engulfment receptor Draper (Drpr) is known to mediate PS recognition in *Drosophila*. However, how Drpr recognizes PS *in vivo* is unclear. Using larval dendritic arborization (da) neurons and phagocytic epidermal cells as a model, we show that the recently discovered *Drosophila* chemokine-like Orion is the responsible PS sensor; it functions as a cell-non-autonomous bridging molecule between PS and Drpr to license phagocytosis. Moreover, the Orion dosage is a key determinant of the sensitivity of phagocytes to PS exposed on neurons. Lastly, mutagenesis analysis reveals evolutionarily conserved sequence motifs that are important for Orion secretion and binding to PS. Thus, our results uncover a missing link in PS-mediated phagocytosis in *Drosophila* and imply conserved mechanisms of phagocytosis of neurons.

Highlights:

- Orion is required for phagocytosis of neurons by binding to PS and Drpr *in vivo*
- Membrane-tethered Orion affects phagocytosis oppositely in neurons and phagocytes
- *orion* dosage determines phagocyte sensitivity to neuronal PS exposure
- Conserved CX_3C and RRY motifs are important for Orion secretion and PS-binding

KEYWORDS

phosphatidylserine, phagocytosis, da neurons, epidermal cells, Orion, Draper, CX_3C, RRY, bridging molecule

INTRODUCTION

Phagocytosis of apoptotic and degenerative neurons is essential for the development and homeostasis of the nervous system (Frost and Schafer, 2016; Galloway et al., 2019). Abnormal phagocytosis is also associated with neuroinflammation and neurodegenerative diseases (Salter and Stevens, 2017). Neuronal debris is recognized and cleared by resident phagocytes of the nervous system through "eat-me" signals exposed on the neuronal surface. A conserved "eat-me" signal is phosphatidylserine (PS), a negatively charged phospholipid normally kept in the inner

43 leaflet of the plasma membrane by P4-ATPase flippases (Leventis and Grinstein, 2010). During
44 neurite degeneration and apoptosis, PS is externalized to the outer surface of neuronal
45 membranes (Nagata, 2018; Sapar et al., 2018; Shacham-Silverberg et al., 2018; Sievers et al.,
46 2003). Exposed PS dominantly triggers phagocytosis of neurons, as demonstrated by the
47 observation that loss of PS flippases in neurons results in PS exposure and neurodegeneration
48 across species (Darland-Ransom et al., 2008; Sapar et al., 2018; Zhu et al., 2012). Recently, PS-
49 mediated phagocytosis was found to drive the degeneration of injured neurites and neurons with
50 certain genetic perturbations (Ji et al., 2022; Sapar et al., 2018). In the central nervous system
51 (CNS), local PS exposure enables microglia-mediated synaptic elimination (Li et al., 2020; Park
52 et al., 2021; Scott-Hewitt et al., 2020). Thus, the regulation and recognition of neuronal PS
53 exposure are critical for the development and homeostasis of the nervous system.

54 Given the importance of PS exposure in phagocytosis, animals have evolved specialized
55 systems to detect PS exposed on cell surfaces. In *C. elegans*, PS sensing is mediated by two
56 receptors that activate two partially redundant phagocytosis pathways: PSR-1 directly interacts
57 with PS through a lysine-rich motif (Yang et al., 2015), whereas CED-1 mediates engulfment of
58 apoptotic cells by interacting with TTR-52, a secreted PS-binding molecule (Wang et al., 2010).
59 While both PSR-1 and CED-1 belong to conserved protein families, TTR-52 is unique to worms.
60 Compared to worms, mammals have a much more complex system containing multiple receptors
61 to sense PS exposure; some of these receptors interact with PS directly while others rely on PS-
62 binding bridging molecules (Bevers and Williamson, 2016; Lemke, 2019). In mammalian brains,
63 BAI1 (Park et al., 2007), TIM-4 (Miyanishi et al., 2007), TREM2 (Wang et al., 2015), and
64 GPR56 (Li et al., 2020) are receptors known to bind PS directly. Other receptors, including
65 MERTK and Axl (Chung et al., 2013; Fourgeaud et al., 2016; Park et al., 2021), αvβ5 integrins
66 (Nandrot et al., 2007), and CR3 (Ma et al., 2012; Paidassi et al., 2008; Schafer et al., 2012), are
67 involved in the phagocytosis of neuronal materials by interacting with their corresponding
68 diffusible PS-binding ligands. Interestingly, these known PS receptors and bridging molecules
69 are either absent or do not function the same way in invertebrates, raising the question of
70 whether conserved mechanisms of PS sensing exist between vertebrates and invertebrates.
71 Although mammalian CED-1 homologues, Jedi-1 and MEGF10, are important for phagocytosis
72 of dead neurons in peripheral ganglia (Wu et al., 2009), whether these molecules are in involved
73 in PS sensing is unknown.

74 *Drosophila* has been an important model organism for studying neuronal phagocytosis. In
75 *Drosophila*, the CED-1 ortholog Draper (Drpr) is the best-known receptor responsible for
76 phagocytosis of neurons (Freeman et al., 2003). Drpr is involved in the clearance of apoptotic
77 neurons during embryonic development (Freeman et al., 2003; Tung et al., 2013), axon and
78 dendrite pruning during neuronal remodeling (Awasaki et al., 2006; Williams et al., 2006),
79 injury-induced neurite degeneration (MacDonald et al., 2006; Tao and Rolls, 2011), and removal
80 of destabilized boutons at neuromuscular junctions (Fuentes-Medel et al., 2009). Neurons with
81 ectopic PS exposure are engulfed by phagocytes in a Drpr-dependent manner (Ji et al., 2022;
82 Sapar et al., 2018), suggesting that Drpr is critical for PS sensing. However, how Drpr recognizes
83 PS is unclear. Although the extracellular domain of Drpr can bind to PS *in vitro* (Tung et al.,
84 2013), it remains unknown whether Drpr directly interacts with PS exposed on neurons *in vivo*.
85 In addition, while detection of PS by diffusible PS sensors is a common mechanism in other
86 species, to date, no such PS-bridging molecules have been identified in *Drosophila*.

87 Recently, the secreted protein Orion was discovered as being required for the
88 developmental pruning and clearance of *Drosophila* mushroom body (MB) axons (Boulanger et
89 al., 2021). Orion is expressed by MB neurons and is required for astrocytes to infiltrate axon
90 bundles and engulf axonal debris. Interestingly, Orion shares a CX_3C motif with mammalian
91 CX3CL1 (also known as fractalkine), which is required for the elimination of synapses in the
92 mouse barrel cortex (Gunner et al., 2019). CX3CL1 is known as a chemokine because of its
93 ability to direct migration of leukocytes and microglia (Bazan et al., 1997; Maciejewski-Lenoir
94 et al., 1999). Thus, Orion represents the first known chemokine-like molecule in *Drosophila* and
95 shares conserved functions with CX3CL1 in the remodeling of the nervous system. However,
96 how Orion and CX3CL1 exactly function in the phagocytosis of neurons is still unknown.

97 In this study, we examined Orion's function in the phagocytosis of *Drosophila* class IV
98 dendritic arborization (C4da) neurons, a well-established *in vivo* model for studying PS-mediated
99 phagocytosis (Han et al., 2014; Ji et al., 2022; Sapar et al., 2018). C4da neurons grow elaborate
100 sensory dendrites on larval epidermal cells (Han et al., 2012), which act as the primary
101 phagocytes during dendrite degeneration and remodeling (Han et al., 2014). Ectopically induced
102 PS exposure on C4da neurons due to loss of P4-ATPase flippases causes dendrite membrane loss
103 in a Drpr-dependent manner (Sapar et al., 2018). PS exposure and phagocytosis-driven dendrite
104 degeneration can also be induced by injury and by removing the NAD^+-producing enzyme

105 Nmnat (Ji et al., 2022), since normal PS asymmetry on the dendrite membrane depends on
106 sufficient NAD^+ levels in the neuron (Sapar et al., 2018; Shacham-Silverberg et al., 2018).

107 Here we present *in vivo* evidence that Orion is a bridging molecule between PS and Drpr.
108 Orion is secreted by peripheral non-neural tissues and serves as a non-autonomous permissive
109 factor for phagocytosis of neurons. Strikingly, accumulation of Orion on neurons dominantly
110 induces phagocytosis even in the absence of PS exposure, while targeting Orion to the surface of
111 phagocytes makes phagocytes blind to PS-exposing neurons. Importantly, the dosage of Orion
112 determines the sensitivity of phagocytes to neuronal PS exposure. Lastly, we establish that the
113 motifs Orion shares with human chemokines and neutrophil peptides are critical for PS binding
114 and protein secretion. These findings reveal key mechanisms of PS recognition in *Drosophila*
115 and imply potentially conserved roles of chemokines in PS-mediated phagocytosis of neurons.

116 **RESULTS**

117 ***orion* is required for phagocytosis of dendrites**

118 To determine if *orion* is involved in phagocytosis of degenerating dendrites of da neurons, we
119 first examined phagocytosis of injured dendrites in the *orion*^{1} mutant, which results in a G to D
120 mutation in the C-termini of both Orion protein isoforms (Figure S1A) and abolishes clearance
121 of pruned axons during MB remodeling (Boulanger et al., 2021). Dendrites were severed from
122 the cell body using laser, and engulfment of the injured dendrites was visualized using MApHS,
123 a pH-sensitive dendritic marker consisting of extracellular pHluorin and intracellular tdTom
124 (Han et al., 2014). Engulfment was signified by the loss of pHluorin signal due to the drop of pH
125 in early phagosomes (Botelho and Grinstein, 2011; Han et al., 2014). Injured dendrites of C4da
126 neurons in the control larvae were completely engulfed by epidermal cells 24 hours (hrs) after
127 injury (AI), as indicated by the loss of pHluorin signals on tdTom-positive dendritic debris
128 dispersed in epidermal cells (Figures 1A-1A", and 1D). Because *orion* is located on the X
129 chromosome, we examined both hemizygous male larvae and homozygous female larvae of
130 *orion*^{1}. In contrast to the wildtype (WT), both groups of *orion*^{1} mutants showed little engulfment
131 of injured dendrites by epidermal cells (Figures 1B-1C", and 1D), as indicated by the presence of
132 pHluorin signals on tdTom-labeled debris of injured dendrites. The debris remained in the
133 original dendritic patterns, which is another sign of impaired engulfment by epidermal cells.
134 These results suggest that *orion* is required for the engulfment of injured dendrites. Since male

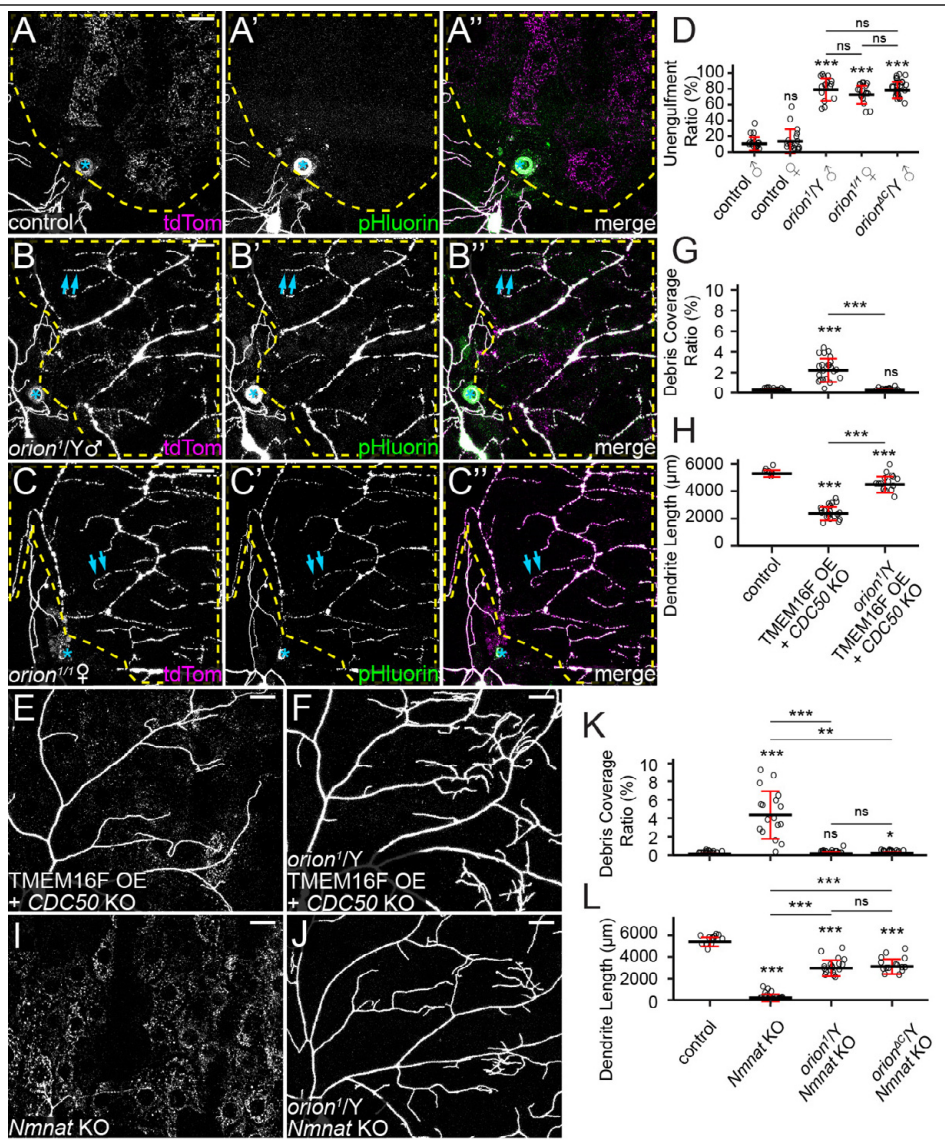

Figure 1: *orion* is required for phagocytosis of dendrites in multiple dendrite degeneration paradigms

(A-C") Partial dendritic fields of ddaC neurons in control (A-A"), *orion*^{1} hemizygous (B-B"), and *orion*^{1} homozygous (C-C") larvae at 22-24 hrs after injury (AI). Yellow dash outlines: territories originally covered by injured dendrites; blue asterisks: injury sites; blue arrows: injured but unengulfed dendrite fragments.

(D) Quantification of unengulfment ratio of injured dendrites (pHluorin-positive debris area/tdTom-positive debris area). n = number of neurons: control males (n = 18, 10 animals); control females (n = 16, 9 animals); *orion*^{1}/Y (n = 16, 8 animals); *orion*$^{1/1}$ (n = 18, 9 animals); *orion*$^{\Delta C}$/Y (n = 25, 12 animals). One-way ANOVA and Tukey's test. (E and F) Partial dendritic fields of TMEM16F OE + CDC50 KO neurons in the wildtype background (E) and orion1 hemizygous background (F).

(G and H) Quantification of debris coverage ratio (percentage of debris area normalized by dendrite area) (G) and dendrite length (H) at 140 hrs after egg laying (AEL). n = number of neurons: control (n = 14, 7 animals); TMEM16F OE + CDC50 KO (n = 22, 11 animals); TMEM16F OE + CDC50 KO in orion1/Y (n = 16, 8 animals). For (G), Kruskal-Wallis (One-way ANOVA on ranks) and Dunn's test, p-values adjusted with the Benjamini-Hochberg method; for (H), One-way ANOVA and Tukey's test.

(I and J) Partial dendritic fields of Nmnat KO neurons in the wildtype background (I) and orion1 hemizygous background (J).

(K and L) Quantification of debris coverage ratio (K) and dendrite length (L) at 120 hrs AEL. n = number of neurons: control (n = 17, 9 animals); Nmnat KO (n = 17, 9 animals); Nmnat KO in orion1/Y (n = 18, 9 animals); Nmnat KO in orionΔC/Y, (n = 16, 9 animals). For (K), Kruskal-Wallis (One-way ANOVA on ranks) and Dunn's test, p-values adjusted with the Benjamini-Hochberg method; for (L), One-way ANOVA and Tukey's test.

In all image panels, neurons were labeled by ppk-MApHS. Scale bars, 25 µm. For all quantifications, *p≤0.05, **p≤0.01, ***p≤0.001; n.s., not significant. The significance level above each genotype is for comparison with the control. Black bar, mean; red bar, SD. See also Figure S1.

135 and female *orion* mutants exhibited similar degrees of engulfment defects (Figure 1D), we used

136 hemizygous male mutants only in subsequent assays.

137 In addition to phagocytosis after injury, C4da dendrites are all pruned and engulfed by
138 epidermal cells during metamorphosis (Han et al., 2014). Consistent with the role of *orion* in
139 axonal pruning of MB neurons (Boulanger et al., 2021), we also confirmed that *orion*^{1} exhibits
140 strong defects in the clearance of pruned dendrites of C4da neurons during metamorphosis
141 (Figure S1B-S1D).

142 The engulfment of injured dendrites by epidermal cells is mediated by PS exposure on
143 dendrites (Ji et al., 2022; Sapar et al., 2018). To test directly if *orion* is required for PS exposure-
144 induced phagocytosis, we examined two additional paradigms in which PS exposure can be more
145 reliably induced and studied. In the first paradigm, PS exposure was ectopically induced in
146 otherwise healthy neurons using a combination of *CDC50* knockout (KO) and TMEM16F
147 overexpression (OE). *CDC50* encodes a chaperone protein required for the activity of P4-
148 ATPases that keep PS in the inner leaflet of the plasma membrane (Segawa and Nagata, 2015).
149 TMEM16F is a mammalian scramblase that mixes PS between the two leaflets of the plasma
150 membrane (Nagata et al., 2016; Suzuki et al., 2010). Dendrites with *CDC50* KO and TMEM16F
151 OE expose PS and shed membrane in a phagocytosis-dependent manner (Sapar et al., 2018).
152 Whereas these neurons showed reduced dendrite length and elevated debris levels in wandering
153 3rd instar larvae with wildtype *orion* (Figures 1E, 1G, and 1H), *orion*^{1} hemizygous males
154 exhibited almost normal dendritic length and no dendritic debris in epidermal cells (Figures 1F-
155 1H), indicating a lack of engulfment by phagocytes.

156 In the second paradigm, we knocked out *Nmnat* to induce dendritic PS exposure and
157 phagocytosis-dependent dendrite degeneration (Ji et al., 2022). *Nmnat* encodes an enzyme
158 involved in the biosynthesis of NAD^{+}, protecting neurites from degeneration (Zhai et al., 2009).
159 The loss of *Nmnat* in C4da neurons results in PS exposure and phagocytosis-dependent dendrite
160 degeneration, likely due to NAD^{+} reduction (Ji et al., 2022). *Nmnat* KO neurons lost most of
161 their dendrites and showed widespread debris in epidermal cells at 120 hrs after egg laying
162 (AEL) (Ji et al., 2022)(Figures 1I, IK, and 1L). In contrast, resembling *drpr* loss-of-function
163 (LOF) (Ji et al., 2022), *orion*^{1} hemizygosity completely rescued the dendrite degeneration of
164 *Nmnat* KO neurons, as indicated by the absence of dendrite debris (Figures 1J-IK). The dendrite
165 length of these neurons was restored to 53% of the WT level (Figures 1I-IL), suggesting that

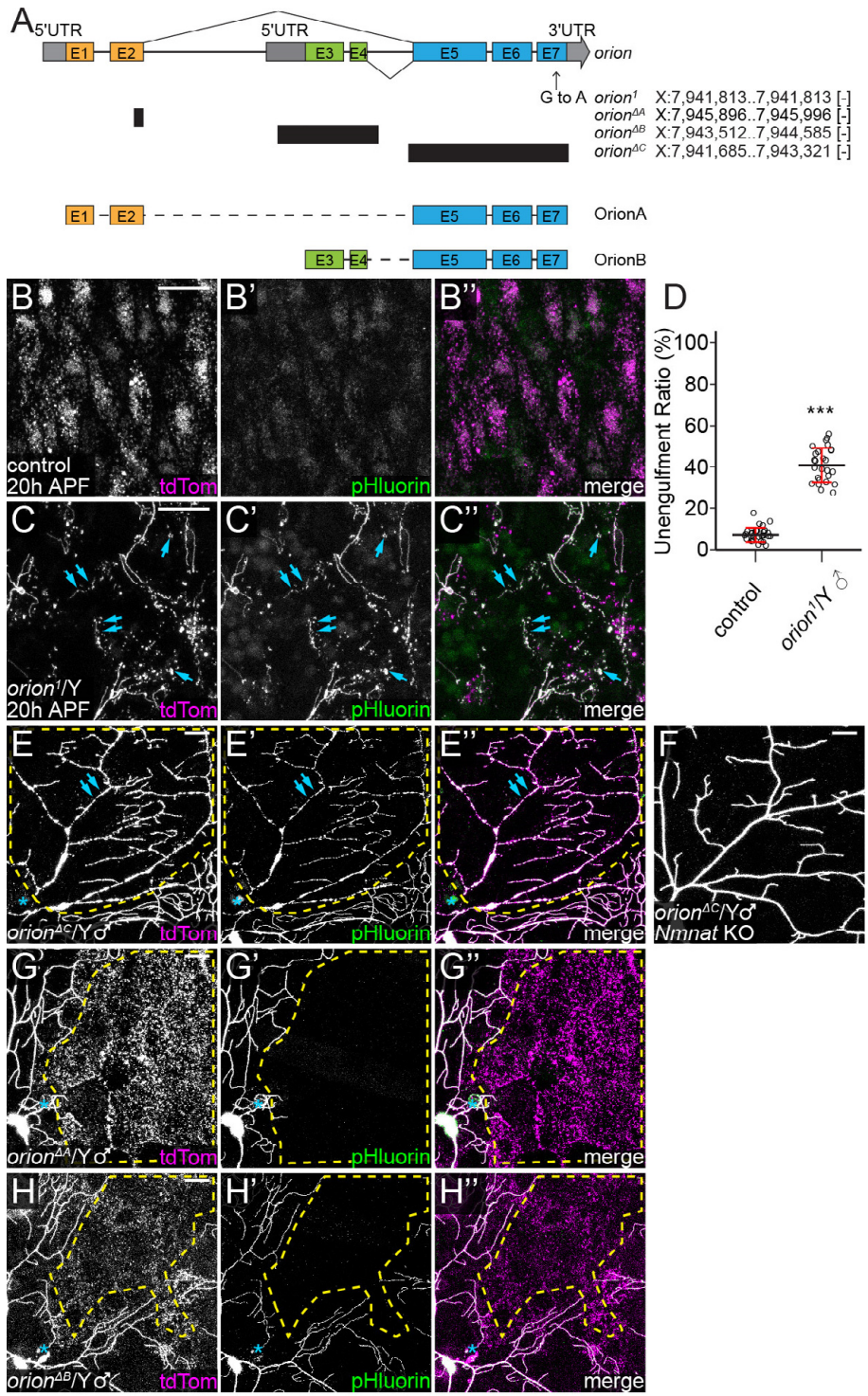

Figure S1: *orion* mutant alleles and engulfment phenotypes

(A) Schematic representation of the *orion* locus in the wildtype and in four different *orion* alleles (*orion*^{1}, *orion*$^{\Delta A}$, *orion*$^{\Delta B}$ and *orion*$^{\Delta C}$). Black bars indicate deleted regions. The two mRNA splicing isoforms of *orion* are also indicated. The *orion* gene annotation is based on Release 6 reference genome assembly.

(B-C") Partial dendritic fields of ddaC neurons at 20 hrs after puparium formation (APF) in wildtype (B-B") and *orion*^{1} hemizygous (C-C") pupae. Blue arrows: unengulfed dendrite fragments.

(D) Quantification of unengulfment ratio of pruned dendrites (area of pHluorin-positive debris/area of tdTom-positive debris) at 19-21 hrs APF. n = number of neurons: control (n = 30, 12 animals); *orion*^{1} hemizygotes (n = 26, 9 animals). Welch's t-test; ***p≤0.001; black bar, mean; red bars, SD.

(E-E") Partial dendritic field of a ddaC neuron in *orion*$^{\Delta C}$ hemizygotes at 23 hrs AI. Blue arrows: injured but unengulfed dendrite fragments.

(F) Partial dendritic field of a *Nmnat* KO neuron in *orion*$^{\Delta C}$ hemizygotes.

(G-H") Partial dendritic fields of ddaC neurons in *orion*$^{\Delta A}$ hemizygotes (G-G"), and *orion*$^{\Delta B}$ hemizygotes (H-H") at 23-24 hrs AI.

In all image panels, neurons were labeled by *ppk-MApHS*. Scale bars, 25 µm. In (E-E") and (G-H"), yellow dash outlines: territories originally covered by injured dendrites; blue asterisks: injury sites.

166 Nmnat may also be involved in dendrite growth or maintenance. Altogether, above data indicate

167 that *orion* is required for PS-mediated phagocytosis of dendrites by epidermal cells.

168 Because *orion*^{1} carries a missense mutation that may not completely abolish Orion
169 function, we compared its properties to those of *orion*$^{\Delta C}$, a predicted null mutation that is missing
170 all three common C-terminal exons of both *orion* isoforms (Figure S1A) (Boulanger et al.,
171 2021). *orion*$^{\Delta C}$ showed similar levels of phagocytosis defects as *orion*^{1} in both injury-induced
172 degeneration (Figures S1E-S1E", and 1D) and *Nmnat* KO-induced degeneration (Figures S1F,
173 and 1K-1L), suggesting that *orion*^{1} has lost most, if not all, of its function (we show later that the
174 Orion^{1} protein has weak activities that can be observed in extremely sensitive assays with

175 overexpressed mutant protein). Since *orion* encodes two isoforms with different N-
176 terminal sequences (Figure S1A), we next asked if one or both isoforms contribute to
177 phagocytosis. Mutations targeting each of the two *orion* isoforms separately (Figure S1A)
178 showed no phagocytosis defects in injury-induced degeneration (Figure S1G-S1H"), suggesting
179 that OrionA and OrionB isoforms are redundant in the phagocytosis of injured dendrites. These
180 results are consistent with the redundant effects of the same mutations in MB neuron axon
181 pruning (Boulanger et al., 2021).

182 **Orion functions cell-non-autonomously**

183 *orion* encodes a secreted protein, raising the question of how it contributes to phagocytosis of
184 dendrites. To determine which tissues express Orion, we generated an *orion* knock-in (KI) allele
185 in which the C-terminus of *orion* is fused in-frame with 4 copies of mNeonGreen2$_{11}$ (mNG2$_{11}$)
186 (Feng et al., 2017), a V5 tag, a self-cleaving F2A sequence (Szymczak et al., 2004), and
187 LexA::VP16 (Chen et al., 2014) (Figure S2A). This allele, abbreviated as *orion*^{KI}, has several
188 purposes: detection of *orion*-expressing cells by LexA::VP16 transcription activity, detection of
189 endogenous Orion proteins by V5 staining, and visualization of endogenous Orion proteins in a
190 tissue-specific manner by reconstitution of mNG2 fluorescence with tissue-specific expression of
191 mNG2$_{1-10}$ (Feng et al., 2017).

192 By using *orion*^{KI} with a *LexAop-GFPnls* reporter, we found that *orion* transcripts are
193 expressed in many peripheral tissues in larvae, including epidermal cells, hemocytes, trachea,
194 and the fat body (Figure 2A-2B). However, *orion* transcription is missing in larval da neurons
195 (Figure 2A, inset), even though a weak *orion* transcription activity was later detected in a subset
196 of da neurons at 5-12 hrs after puparium formation (APF) (Figures S2B-S2B"), when some da

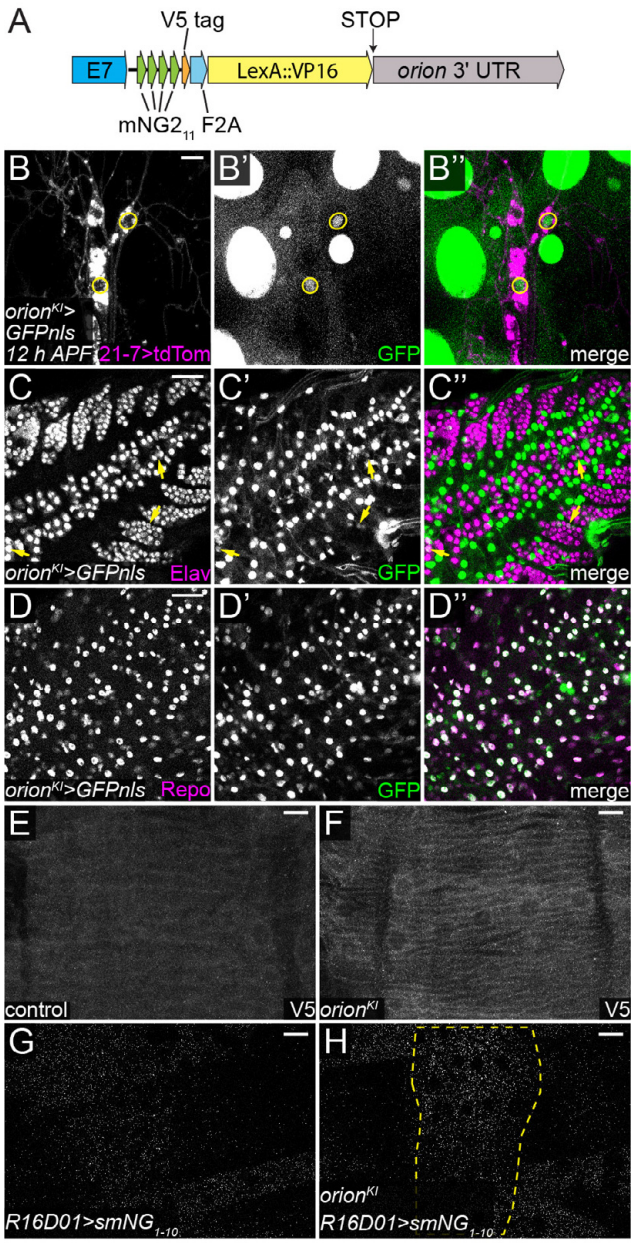

Figure S2: Orion functions cell-non-autonomously

(A) Schematic representation of the *orion*^{KI} allele.

(B-B") GFPnls expression driven by *orion-LexA* in ddaC and ddaE neurons at 12 hrs APF. Yellow circles indicate nuclei of ddaC and ddaE neurons. Neurons were labeled by *21-7-Gal4>CD4-tdTom*.

(C-D") GFPnls expression driven by *orion-LexA* in the larval ventral nerve cord (VNC). Nuclei of neurons are labeled by Elav staining (C-C"); glial nuclei are labeled by Repo staining (D-D"). Yellow arrows (C-C"): a small number of neurons expressing *orion*.

(E-F) V5 staining of larval body walls in the wildtype control (w^{1118}) (E) and *orion*^{KI} (F).

(G-H) Signals of reconstituted mNG in control (G) and *orion*^{KI} (H) epidermal cells. Secreted mNG$_{1-10}$ (smNG$_{1-10}$) was expressed in patches of epidermal cells (outlined in H) driven by *R16D01-Gal4*.

Scale bars, 10 µm (B) and 25 µm (C-H).

197 neurons die and others undergo dendritic pruning (Williams and Truman, 2005a). In the central
198 nervous system, we found that *orion* was transcribed in most glial cells and in a small subset of
199 neurons at the wandering 3rd instar larval stage (Figure S2C-S2D"). Despite the robust
200 LexA::VP16 activity in *orion*^{KI}, Orion proteins appear to be expressed at a low level. Using V5
201 staining, we could observe only weak Orion signals on the larval epidermis (Figures S2E and
202 S2F). By expressing secreted mNG2$_{1-10}$ in a patch of epidermal cells (in the R16D01 domain),
203 we also detected weak Orion-mNG2 signals in what appear to be the secretory compartments of
204 epidermal cells (Figures S2G and S2H).

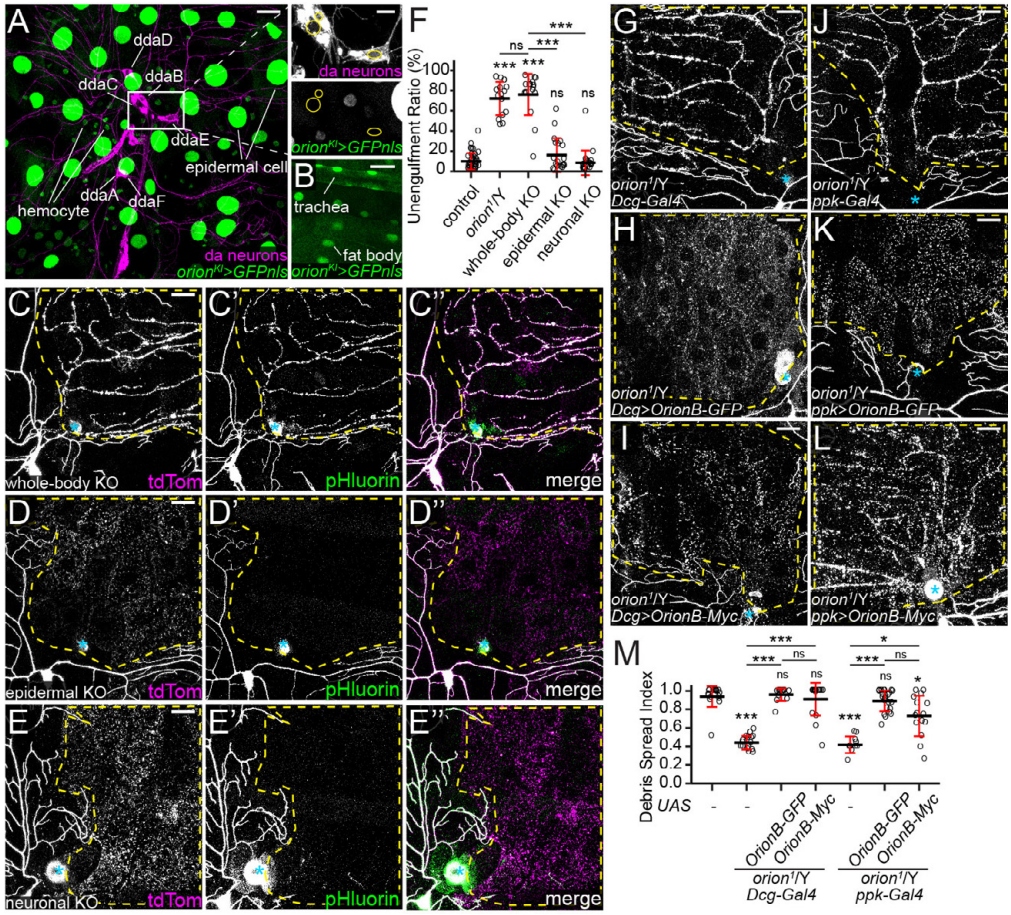

Figure 2: Orion functions cell-non-autonomously

(A-B) GFPnls expression driven by *orion-LexA* (*orion*^{KI}) in epidermal cells, hemocytes (A), trachea, and fat body (B), but not in da neurons (A, insets). Yellow circles indicate nuclei of ddaB, ddaC, and ddaE neurons (A). Scale bars, 25 µm (A), 10 µm (A insets), and 50 µm (B).

(C-E") Partial dendritic fields of neurons in whole-body *orion* KO (C-C"), epidermal *orion* KO (D-D"), and neuronal *orion* KO (E-E") at 22-24 hrs AI.

(F) Quantification of unengulfment ratio of injured dendrites. n = number of neurons: control and *orion*^{1}/Y (same dataset as in Figure 1D); whole-body *orion* KO (n = 18, 10 animals); epidermal *orion* KO (n = 19, 11 animals); neuronal *orion* KO (n = 21, 11 animals). One-way ANOVA and Tukey's test.

(G-L) Partial dendritic fields of ddaC neurons in *orion*^{1} hemizygotes with fat body Gal4 (G), with OrionB-GFP OE in the fat body (H), with OrionB-Myc OE in the fat body (I), with neuron Gal4 (J), with OrionB-GFP OE in neurons (K), and with OrionB-Myc OE in neurons (L) at 22-24 hrs AI.

(M) Quantification of debris spread index of injured dendrites (area ratio of all 15 pixel x 15 pixel squares that contained dendrite debris in the region of interest). n = number of neurons: wildtype control (n = 18, 10 animals); *Dcg-Gal4* in *orion*^{1}/Y (n = 16, 9 animals); *Dcg>OrionB-GFP* in *orion*^{1}/Y (n = 13, 7 animals), *Dcg>OrionB-Myc* in *orion*^{1}/Y (n = 17, 10 animals); *ppk-Gal4* in *orion*^{1}/Y (n = 10, 6 animals); *ppk>OrionB-GFP* in *orion*^{1}/Y (n = 24, 12 animals); *ppk>OrionB-Myc* in *orion*^{1}/Y (n = 15, 9 animals). Kruskal-Wallis (One-way ANOVA on ranks) and Dunn's test, p-values adjusted with the Benjamini-Hochberg method.

Neurons were labeled by *21-7>UAS-CD4-tdTom* (A-B), *ppk-MApHS* (C-E"), *ppk-CD4-tdTom* (G, H, I), and *ppk>CD4-tdTom* (J, K, L). In (C-E") and (G-L), yellow dash outlines: territories originally covered by injured dendrites; blue asterisks: injury sites; scale bars, 25 µm. For all quantifications, *p≤0.05, ***p≤0.001; n.s., not significant. The significance level above each genotype is for comparison with the control. Black bar, mean; red bar, SD. See also Figure S2.

To investigate whether *orion* is required in specific tissues for phagocytosis of injured dendrites, we knocked out *orion* in either neurons or epidermal cells using CRISPR-TRiM, a method of tissue-specific mutagenesis that relies on a tissue-specific Cas9 and ubiquitously

208 expressed guide RNAs (gRNAs) (Poe et al., 2019). As a control, knocking out *orion* with a
209 ubiquitous Cas9 (*Act5C-Cas9*) (Port et al., 2014) faithfully replicated the phagocytosis defects of
210 *orion*^{1} (Figures 2C-2C", and 2F), demonstrating the effectiveness of CRISPR-TRiM. However,
211 *orion* KO in either da neurons alone (with *SOP-Cas9*; (Poe et al., 2019)) or in epidermal cells
212 alone (with *shot-Cas9*; (Ji et al., 2022)) did not interfere with the engulfment of injured dendrites
213 (Figures 2D-2E", and 2F).

214 The lack of effect of *orion* KO in da neurons or in epidermal cells suggests that Orion
215 functions cell-non-autonomously. We further tested this idea by asking whether supplying Orion
216 in the extracellular space is sufficient to rescue the impaired engulfment of injured dendrites in
217 *orion* mutants. Extracellular Orion supply was achieved by overexpressing Orion in the fat body,
218 which can efficiently secrete proteins into the hemolymph (Sapar et al., 2018). We quantified the
219 degree of engulfment by the spread of dendrite debris in the epidermis: Successful engulfment
220 will cause an even dispersion of the debris whereas failure of engulfment will result in dendrite
221 fragments remaining in the original dendrite pattern. Because overexpression (OE) of OrionA in
222 the fat body caused early larval lethality, we chose to use two OrionB transgenes in these rescue
223 experiments: one tagged with Myc constructed in an intermediate-expression vector (Boulanger
224 et al., 2021), and the other tagged with GFP constructed in a high-expression vector (Sapar et al.,
225 2018). Both OrionB transgenes overexpressed in the fat body rescued the engulfment of injured
226 dendrites in *orion*^{1} hemizygotes to the wildtype level (Figures 2G-2I, and 2M).

227 We next checked whether OrionB secreted from neurons is sufficient to rescue the
228 engulfment defects in the *orion*^{1} mutant. Interestingly, neuronal expression of OrionB-GFP fully
229 rescued the engulfment defects (Figure 2K, and 2M), while OrionB-Myc did not rescue
230 engulfment to the wildtype level (Figure 2L, and 2M), consistent with the predicted higher
231 expression of OrionB-GFP.

232 Together, these results indicate that Orion is primarily expressed in non-neural tissues in
233 the periphery and functions cell-non-autonomously for the engulfment of dendrites. Our data
234 also suggest that, compared to the fat body, neurons are a less effective source of Orion for
235 engulfment of dendrites.

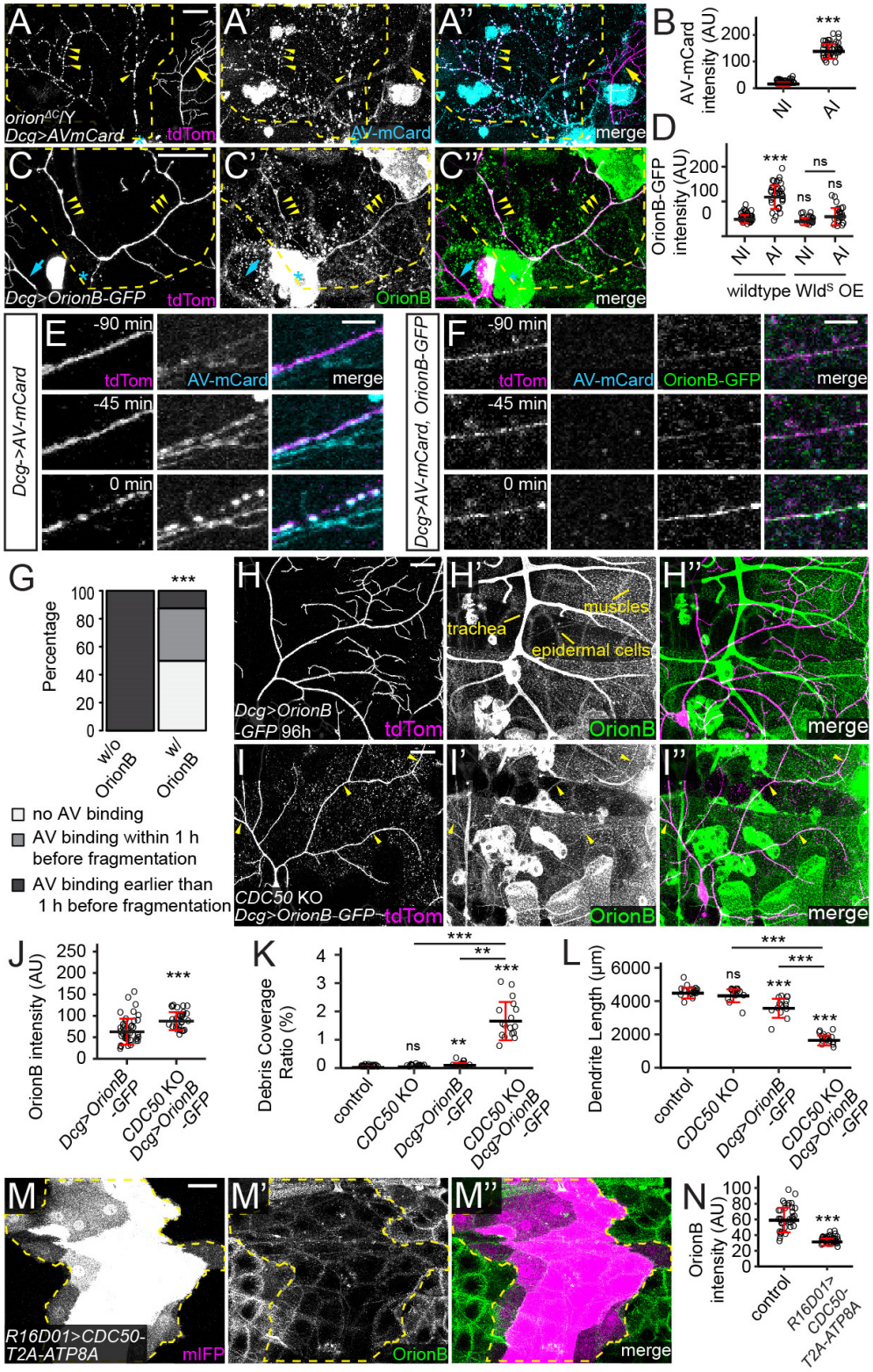

Figure 3: PS exposure is necessary and sufficient for Orion to bind to the cell surface

(A-A") Labeling of injured dendrites of a ddaC neuron by AV-mCard at 23 hrs AI in *orion*$^{\Delta C}$ hemizygous larvae. Yellow arrowheads: injured dendrites with AV-mCard labeling; yellow arrows: uninjured dendrites lacking AV-mCard labeling.

(B) Quantification of AV-mCard binding on dendrites. AV-mCard intensities were measured on both uninjured (NI) and injured (AI) dendrites. n = number of measurements: NI (n = 39, 8 animals); AI (n = 39, 8 animals). Welch's t-test.

Continue in next page.

Figure 3 legend continued.

(C-C") Labeling of injured dendrites of a ddaC neuron by Orion-GFP at 6 hrs AI in wildtype larvae. Yellow arrowheads: injured dendrites with OrionB-GFP labeling.

(D) Quantification of Orion-GFP binding on dendrites of wildtype and Wld^S OE neurons. n = number of measurements: wildtype NI (n = 39, 10 animals); wildtype AI (n = 36, 10 animals); Wld^S OE NI (n = 22, 6 animals); Wld^S OE AI (n = 23, 6 animals). Kruskal-Wallis (One-way ANOVA on ranks) and Dunn's test, p-values adjusted with the Benjamini-Hochberg method.

(E-F) Time series of injured dendrites of ddaC neurons from 90 min before fragmentation to the moment of fragmentation, with only AV-mCard expressed (E) or both OrionB-GFP and AV-mCard co-expressed (F) by the fat body. Time stamps are relative to the frame of dendrite fragmentation.

(G) Percentages of injured dendrites showing no AV binding, AV binding within 1 hr before fragmentation, AV binding earlier than 1 hr before fragmentation. n = number of measurements: w/o OrionB OE (n = 9, 5 animals); w/ OrionB OE (n = 8, 3 animals). Fisher's exact test.

(H-I") Distribution of fat body-derived OrionB-GFP with wildtype (H-H") and *CDC50* KO (I-I") dendrites at 96 hrs AEL. Peripheral tissues showing OrionB-binding are labeled in (H'). Yellow arrowheads indicate OrionB-binding on *CDC50* KO dendrites (I-I").

(J) Quantification of OrionB-GFP binding on wildtype and *CDC50* KO dendrites. n = number of measurements: *Dcg>OrionB-GFP* (n = 41, 7 animals); *CDC50* KO + *Dcg>OrionB-GFP* (n = 29, 6 animals). Welch's t-test.

(K-L) Quantification of debris coverage ratio (K) and dendrite length (L) at 96 hrs AEL. n = number of neurons: control (n = 17, 9 animals); *CDC50* KO (n = 15, 8 animals); *Dcg>OrionB-GFP* (n = 13, 8 animals); *CDC50* KO + *Dcg>OrionB-GFP* (n = 17, 9 animals). For (K), Kruskal-Wallis (One-way ANOVA on ranks) and Dunn's test, p-values adjusted with the Benjamini-Hochberg method; for (L), one-way ANOVA and Tukey's test .

(M-M") OrionB-GFP binding on epidermal cells that expressed *CDC50-T2A-ATP8A*. Yellow dash outlines: *CDC50-T2A-ATP8A* overexpressing region.

(N) Quantification of OrionB-GFP binding on wildtype epidermal cells and *CDC50-T2A-ATP8A* OE epidermal cells. n = number of measurements: control (n = 36, 9 animals); *R16D01>CDC50-T2A-ATP8A* (n = 36, 9 animals). Welch's t-test.

In (A-A") and (C-C"), yellow dash outlines: territories originally covered by injured dendrites; blue asterisks: injury sites. Neurons were labeled by *ppk-MApHS* (A-A" and E-E"), and *ppk-CD4-tdTom* (C-C", F-F" and H-I"). Scale bars, 25 μm (A-A", C-C", H-I"), 5 μm (E-F), and 50 μm (M-M"). For all quantifications, **p≤0.01, ***p≤0.001; n.s., not significant. The significance level above each genotype is for comparison with the control. Black bar, mean; red bar, SD. See also Movie S1-S3 and Figure S3.

To further understand the engulfment defects in *orion* mutants, we examined PS exposure on injured dendrites. We used fat body-derived Annexin V-mCardinal (AV-mCard) as a PS sensor; it labels injured but not healthy dendrites (Sapar et al., 2018). AV-mCard robustly labeled dendrite fragments in $orion^{\Delta C}$ mutant larvae at 24 hrs AI (Figure 3A-3B), suggesting that *orion* LOF does not interfere with PS exposure on injured dendrites and that Orion likely functions downstream of PS exposure in the phagocytosis pathway.

Because Orion is a secreted protein, we asked where Orion is located during engulfment. Similar to AV-mCard, we observed strong enrichment of fat body-derived OrionB-GFP on injured dendrites at 4-6 hrs AI (Figure 3C-3D, and Movie S1), a timepoint when injured dendrites expose high levels of PS (Sapar et al., 2018). Wld^S, a transgene that carries NMNAT1

activity, suppresses fragmentation and PS exposure of injured dendrites when overexpressed in neurons (Ji et al., 2022; Sapar et al., 2018). Interestingly, Wld^S OE also efficiently suppressed OrionB-GFP enrichment on injured dendrites (Figures S3A-S3A", and 3D), indicating that PS exposure may be required for Orion binding.

To test directly the possibility that Orion interacts with PS on injured dendrites, we asked whether OrionB can compete with AV-mCard for binding to injured dendrites, given that AV binds to PS directly (Leventis and Grinstein, 2010). Using long-term time-lapse imaging (Ji and Han, 2020), we found that fat body-derived AV-mCard accumulated on injured dendrites at least 60 minutes before dendrite fragmentation (9/9 movies) (Figures 3E and 3G, and Movie S2). However, when both OrionB-GFP and AV-mCard were co-expressed by the fat body, OrionB-GFP was detected on injured dendrites long before fragmentation (8/8 movies), while AV-mCard did not bind the same injured dendrite in half of the cases (4/8 movies) (Figures 3F and 3G, and Movie S3). In most cases where AV-mCard was observed on injured dendrites (3/4 movies), the labeling only appeared right at the time of dendrite fragmentation (Figure 3G), when PS exposure is at its peak (Sapar et al., 2018). These results suggest that Orion can outcompete AV

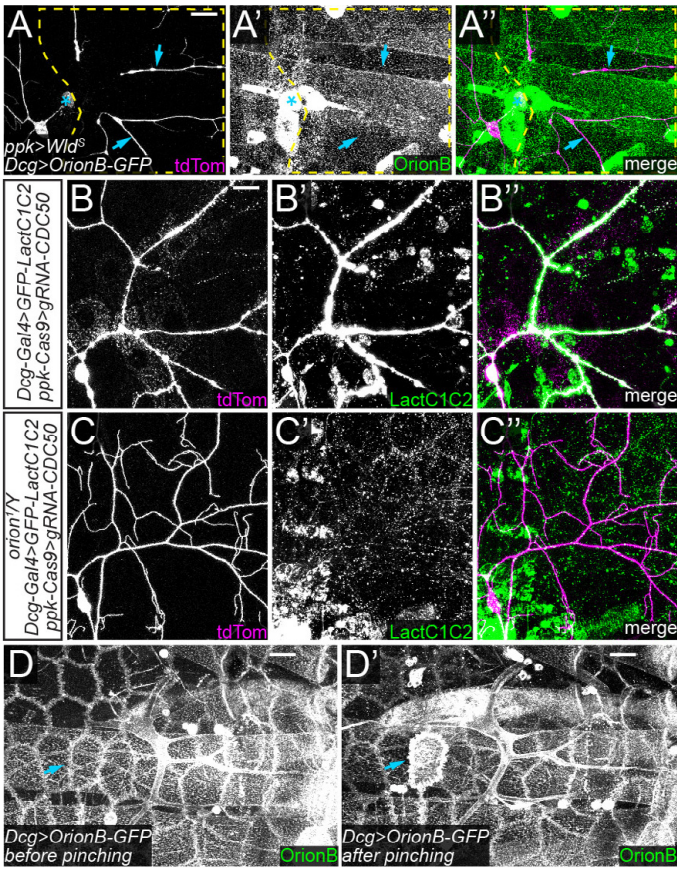

Figure S3: PS exposure is necessary and sufficient for Orion to bind to the cell surface

(A-A") Lack of OrionB-GFP labeling on injured dendrites of a ddaC neuron with Wld^S OE at 6 hrs AI. Yellow dash outlines: territories originally covered by injured dendrites; blue asterisks: injury sites; blue arrows: injured dendrites lacking OrionB-GFP labeling.

(B-C") *CDC50* KO neurons in the presence of fat body-derived GFP-LactC1C2 in control (B-B") and *orion*^{1} hemizygous (C-C") larvae.

(D-D') OrionB-GFP binding on epidermal cells before (D) and after (D') gentle pinching. Blue arrows indicate enhanced OrionB binding.

Neurons were labeled by *ppk-CD4-tdTom* (A-C"). In all image panels, scale bars, 25 µm.

262 for binding to injured dendrites, most likely by directly interacting with PS on the surface of
263 injured dendrites.

264 To test if neuronal PS exposure is sufficient to induce Orion binding, we ectopically
265 induced dendritic PS exposure by knocking out *CDC50* in neurons (Sapar et al., 2018).
266 Distribution of fat body-derived OrionB-GFP was examined at 96 hrs AEL, a time when *CDC50*
267 KO alone is not yet sufficient to cause membrane loss of dendrites (Figures 3K and 3L). OrionB-
268 GFP showed little binding to wildtype dendrites (Figures 3H-3H", and 3J) but bound robustly to
269 *CDC50* KO dendrites (Figures 3I-3J) at this stage. Interestingly, the presence of OrionB-GFP
270 caused appreciable degeneration of *CDC50* KO dendrites, as indicated by the drastically
271 increased dendrite debris and shortened total dendrite length (Figures 3K and 3L). These results
272 suggest that Orion is recruited to PS-exposing dendrites and OrionB binding on dendrites
273 potentiates epidermal engulfment.

274 The PS-binding C1C2 domain of mouse Lactadherin (LactC1C2) has been used as a PS
275 sensor in multiple systems (Hanayama et al., 2002; Mapes et al., 2012; Sapar et al., 2018;
276 Shacham-Silverberg et al., 2018). We previously reported that fat body-derived LactC1C2 not
277 only labels degenerating dendrites but also promotes degeneration of *CDC50* KO dendrites
278 (Sapar et al., 2018) (Figures S3B-S3B"). Surprisingly, this degeneration was completely
279 suppressed in the *orion*^{1} hemizygotes (Figures S3C-S3C"), suggesting that the effects of
280 LactC1C2 are mediated by Orion.

281 We also noticed that OrionB-GFP binds to the surface of several other peripheral tissues,
282 including epidermal cells, muscles, and trachea (Figures 3H-3H"). The OrionB-GFP binding on
283 epidermal cells was enhanced after we gently pinched the larval body wall, which is expected to
284 mildly disrupt the epidermal cell membrane (Figures S3D-S3D'). We next examined whether
285 these non-neuronal Orion bindings are also mediated by PS. To block PS exposure, we
286 overexpressed ATP8A, an ortholog of the PS-specific flippase TAT-1 (Darland-Ransom et al.,
287 2008; Wehman et al., 2011). Overexpression of ATP8A in da neurons is sufficient to suppress
288 PS exposure and the associated dendrite degeneration caused by *Nmnat* KO (Ji et al., 2022). The
289 P4-ATPase chaperone CDC50 was co-expressed with ATP8A in a patch of epidermal cells to
290 facilitate ATP8A trafficking. Epidermal overexpression of ATP8A and CDC50 drastically

291 suppressed OrionB-GFP binding on the surface of epidermal cells (Figures 3M-3N), suggesting
292 that this binding is PS-exposure dependent.

293 Together, our results suggest that PS exposure is both required and sufficient for Orion to
294 bind to the cell surface of both neuronal and non-neural cells.

295 **Orion functions upstream of Drpr**

296 Because *drpr* is the only other gene known to be required for epidermal engulfment of PS-
297 exposing dendrites (Ji et al., 2022; Sapar et al., 2018), we wondered if Orion and Drpr act in the
298 same pathway. We found that *orion*^{1} hemizygous and *drpr* mutant larvae exhibited similar
299 degrees of near complete phagocytosis deficiency in injury-induced dendrite degeneration, as
300 indicated by the portion of unengulfed MApHS-labeled debris (Figures 4A- 4B). Both genotypes
301 also completely rescued *Nmnat* KO-induced dendrite degeneration, as reflected by the debris
302 level and the dendrite length (Figures 4C and 4D). We further asked whether removing both *drpr*
303 and *orion* produces stronger phagocytosis defects than the loss of either. Using CRISPR-TRiM,
304 we induced whole-body KO of *orion* and *drpr* individually and together. Injured dendrites
305 showed indistinguishable levels of near complete blockage of engulfment in all three genotypes
306 at 24 hrs AI (Figures 4E-4G), suggesting that *orion* and *drpr* function in the same genetic
307 pathway.

308 To elucidate the epistatic relationship between *orion* and *drpr*, we tested whether the
309 Orion-PS interaction depends on Drpr and whether gain-of-function (GOF) of one gene can
310 rescue the LOF of the other. At 4-5 hrs AI, OrionB-GFP bound to injured dendrites in wildtype
311 and *drpr* null larvae at similar levels (Figure 4H-4I), demonstrating that Orion does not need
312 Drpr for binding to PS. Two observations further suggest that Orion GOF cannot compensate for
313 the loss of *drpr* in engulfment: First, overexpression of Orion in the fat body did not rescue the
314 engulfment of injured dendrites in *drpr* mutants at 24 hrs AI (Figures S4A and 4J); and second,
315 the degeneration of *CDC50* KO dendrites induced by OrionB-GFP (Figure 3I-3L) was absent in
316 *drpr* mutants (Figures S4B-S4D). To test the converse possibility that *drpr* GOF can rescue
317 *orion* LOF, we overexpressed Drpr in a patch of epidermal cells in the posterior hemisegment
318 (driven by *hh-Gal4*) of *orion*$^{\Delta C}$ hemizygotes. Interestingly, Drpr OE restored engulfment of
319 injured dendrites, as indicated by the dispersion of dendrite debris specifically in the *hh* domain

320 (Figures 4K-4L). These data indicate that Drpr functions downstream of Orion, and that high

321 levels of Drpr can compensate for the loss of Orion in phagocytosis.

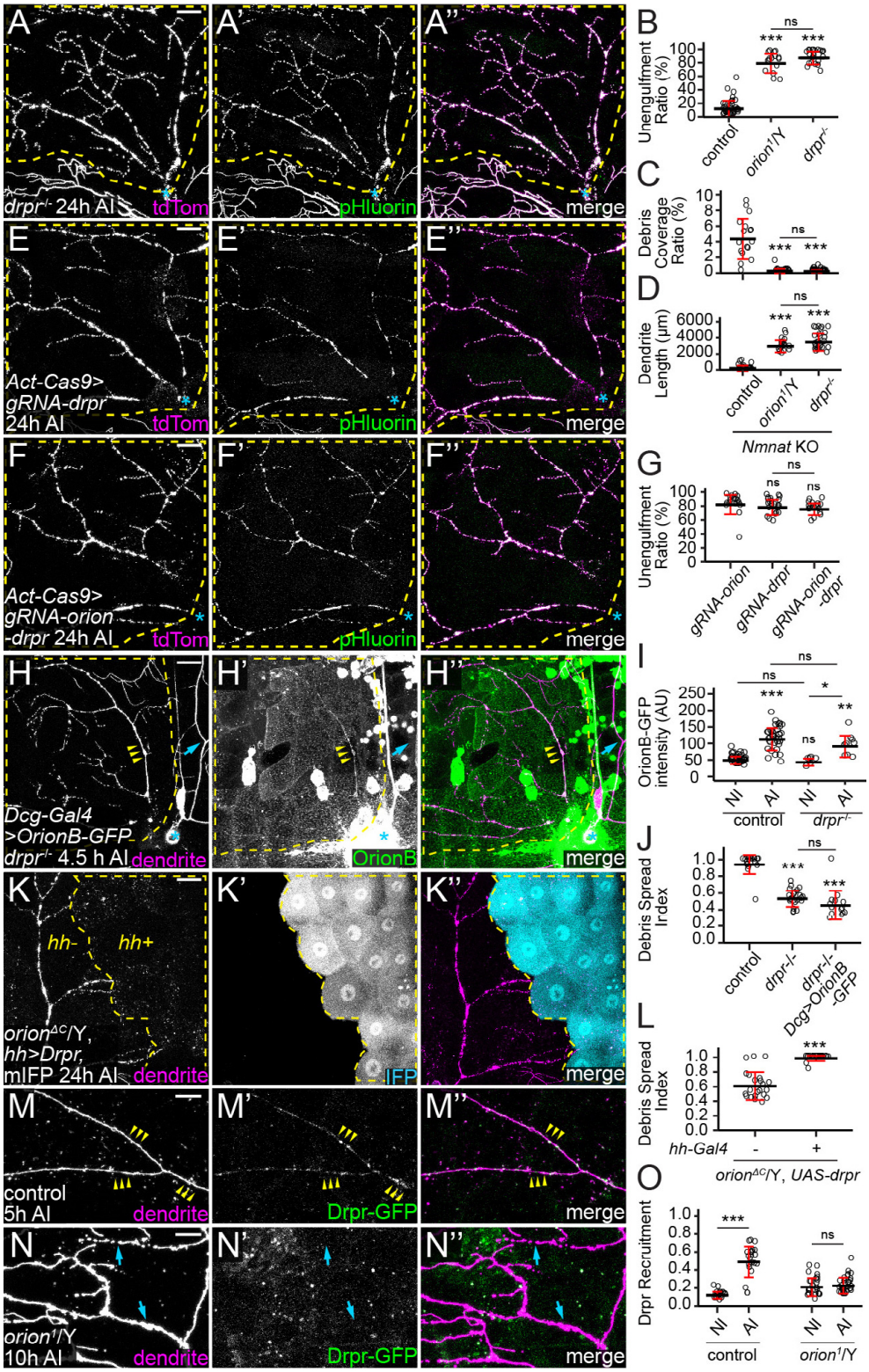

Figure 4: Orion functions upstream of Drpr

(A-A") Partial dendritic fields of a ddaC neuron in *drpr*$^{-/-}$ at 24 hrs AI.

(B) Quantification of unengulfment ratio of injured dendrites. n = number of neurons: control and *orion*^{1}/Y (same dataset as in Figure 1D); *drpr*$^{-/-}$ (n = 23, 10 animals). One-way ANOVA and Tukey's test.

(C-D) Quantification of debris coverage ratio (C) and dendrite length (D) at 120 hrs AEL. n = number of neurons: *Nmnat* KO in wildtype and in *orion*^{1}/*Y* (same dataset as in Figure 1K); *Nmant* KO in *drpr*$^{-/-}$ (n = 28, 14 animals). Kruskal-Wallis (One-way ANOVA on ranks) and Dunn's test, p-values adjusted with the Benjamini-Hochberg method.

Continue in next page.

Figure 4 legend continued.

(E-F") Partial dendritic fields of ddaC neurons at 24 hrs AI with whole-body *drpr* KO (E-E"), and *drpr+orion* double KO (F-F").

(G) Quantification of unengulfment ratio of injured dendrites. n = number of neurons: *orion* KO (same dataset as in Figure 2F); *drpr* KO (n = 23, 12 animals); *orion+drpr* double KO (n = 19, 10 animals). One-way ANOVA and Tukey's test.

(H-H") Labeling of injured dendrites of a ddaC neuron by OrionB-GFP in $drpr^{-/-}$ at 4.5 hrs AI. Yellow arrowheads: injured dendrites with OrionB-GFP labeling; blue arrows: uninjured dendrites lacking OrionB-GFP binding.

(I) Quantification of Orion-GFP binding on dendrites in the wildtype and the $drpr^{-/-}$ larvae. n = number of measurements: wildtype NI and wildtype AI (same dataset as in Figure 3D); $drpr^{-/-}$ NI (n = 6, 2 animals); $drpr^{-/-}$ AI (n = 9, 3 animals). Kruskal-Wallis (One-way ANOVA on ranks) and Dunn's test, p-values adjusted with the Benjamini-Hochberg method.

(J) Quantification of debris spread index of injured dendrites at 22-24 hrs AI. n = number of neurons: control (same dataset as in 2M); $drpr^{-/-}$ (n = 23, 10 animals); $drpr^{-/-}$ + *Dcg>OrionB-GFP* (n = 14, 7 animals). One-way ANOVA and Tukey's test.

(K-K") Engulfment of injured dendrites in an $orion^{\Delta C}$ hemizygous larva with Drpr overexpressed in the *hh* domain. Yellow dash outlines: *hh>Drpr, mIFP* region.

(L) Quantification of debris spread index of injured dendrites at 22-24 hrs AI in region without Drpr OE and region with Drpr OE in $orion^{\Delta C}/Y$. n = number of neurons: region without Drpr OE (n = 22, 12 animals); and region with Drpr OE (n = 24, 12 animals). Welch's t-test.

(M-N") Distribution of Drpr-GFP in the presence of injured dendrites in control at 5 hrs AI (M-M") and in $orion^{1}/Y$ at 10 hrs AI (N-N"). Yellow arrowheads (M-M"): injured dendrites with Drpr-GFP recruitment; bule arrowheads (N-N"): injured dendrites lacking Drpr-GFP recruitment.

(O) Quantification of Drpr-GFP recruitment (Drpr-GFP-positive area on dendrites/total dendrite area). n = measurements: control NI (n = 20, 12 animals); control AI (n = 21, 12 animals); $orion^{1}/Y$ NI (n = 27, 8 animals); $orion^{1}/Y$ AI (n = 31, 8 animals). Welch's t-test.

Neurons were labeled by *ppk-MApHS* (A-A", E-E" and F-F"), and by *ppk-CD4-tdTom* (H-H", K-K", and M-N"). In (A-A"), (E-E"), (F-F") and (H-H"), yellow dash outlines: territories originally covered by injured dendrites; blue asterisks: injury sites. Scale bars, 25 μm (A-A", E-E", F-F", H-H", K-K") and 10 μm (M-N"). For all quantifications, *p≤0.05, **p≤0.01, ***p≤0.001; n.s., not significant. The significance level above each genotype is for comparison with the control. Black bar, mean; red bar, SD. See also Figure S4.

To further understand how *orion* LOF affects Drpr, we examined the distribution of Drpr protein by live imaging. For this purpose, we generated a knock-in allele of *drpr* so that the C-terminus of endogenous Drpr is tagged by mNeonGreen (mNG) (Shaner et al., 2013) (Figure S4E). To further boost the Drpr signal, we also made a Drpr-GFP transgene that contains a genomic fragment of the *drpr* locus tagged with GFP at the Drpr C-terminus (Figure S4E). Combining a copy of each of *drpr-mNG* and *drpr-GFP* (referred to as simply *drpr-GFP* because both fluorescent proteins are green), we were able to see robust Drpr recruitment to injured dendrites prior to dendrite fragmentation in the wildtype (Figures 4M-4M" and 4O). However, this recruitment was abolished in the $orion^{1}$ hemizygote, even though injured dendrites showed signs of degeneration, such as thinning and blebbing (Figures 4N-4O). These results suggest that Orion regulates Drpr's response to degenerating dendrites after injury.

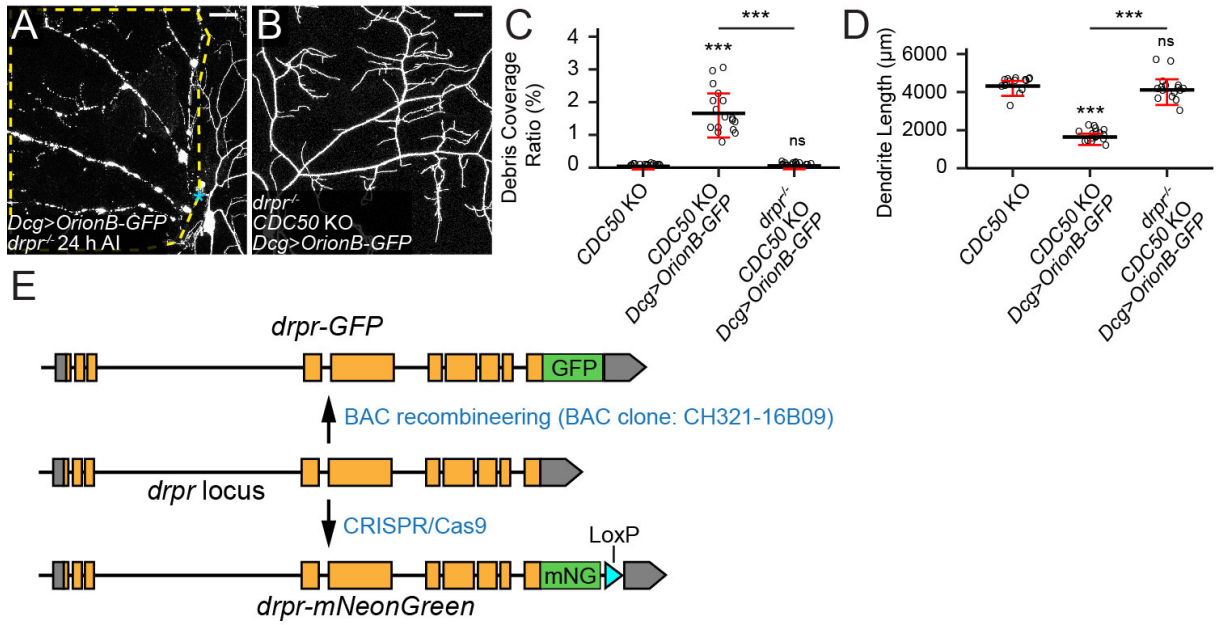

Figure S4: Orion functions upstream of Drpr

(A) Partial dendritic fields of an injured ddaC neuron with OrionB-GFP OE in fat body in the *drpr*$^{-/-}$ background at 24 hrs AI.

(B) Partial dendritic fields of a *CDC50* KO neuron with OrionB-GFP OE in fat body in the *drpr*$^{-/-}$ background.

(C-D) Quantification of debris coverage ratio (C) and dendrite length (D). n = number of neurons: *CDC50* KO and *CDC50* KO + *Dcg>OrionB-GFP* (96 hrs AEL, same dataset as in Figure 3K); *drpr*$^{-/-}$ + *CDC50* KO + *Dcg>OrionB-GFP* (120 hrs AEL, n = 16, 8 animals). For (C), Kruskal-Wallis (One-way ANOVA on ranks) and Dunn's test, p-values adjusted with the Benjamini-Hochberg method; for (D), one-way ANOVA and Tukey's test; ***$p \leq 0.001$; n.s., not significant. The significance level above each genotype is for comparison with the control. Black bar, mean; red bars, SD.

(E) Schematic representation of Drpr-GFP and Drpr-mNG. Yellow boxes indicate exons, grey boxes indicate untranslated regions.

For both image panels, neurons were labeled by *ppk-CD4-tdTom*. Scale bars, 25 µm.

Orion mediates the interaction between PS and Drpr

Because Orion interacts with PS and functions upstream of Drpr, we wondered whether Orion mediates PS recognition by interacting with Drpr. We first tested whether Orion could bind to Drpr *in vivo* by expressing Drpr in a patch of epidermal cells (driven by *R16D01-Gal4*). Fat body-derived OrionB-GFP was found to accumulate specifically on the surface of these Drpr OE cells in wandering 3rd instar larvae (Figures 5A-5B). Interestingly, some epidermal cells with higher OrionB-GFP enrichment (due to higher Gal4 activities) extruded into neighboring epidermal cells that had low or no OrionB-GFP enrichment (Figures S5A-S5A"). We interpret these extrusions as engulfment of high-OrionB cells by low-OrionB cells. To exclude the possibility that OrionB-GFP was recruited by other cell-surface molecules on epidermal cells as

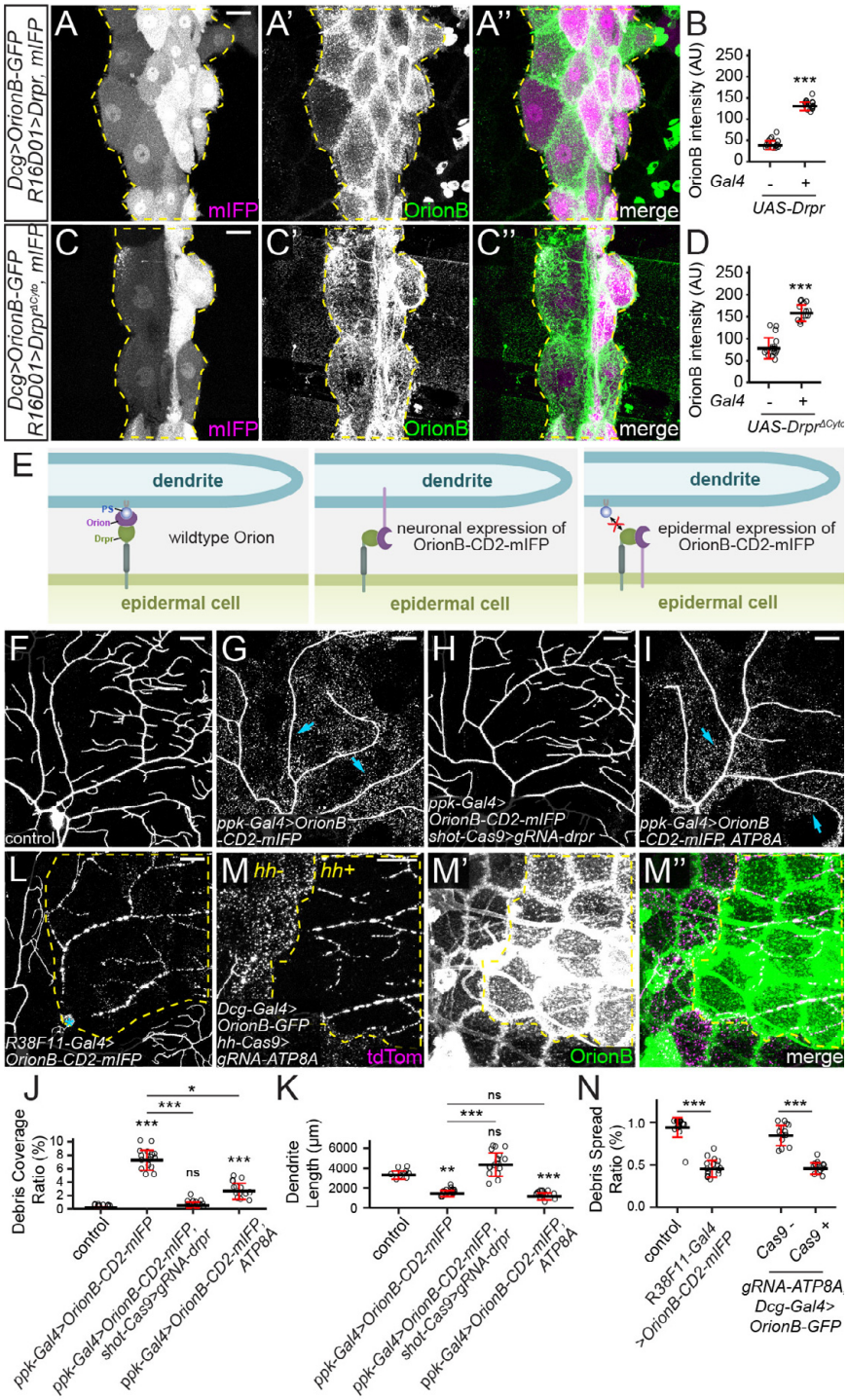

Figure 5: Orion mediates the interaction between PS and Drpr

(A-A") Distribution of fat body-derived OrionB-GFP with Drpr overexpressed in a patch of epidermal cells driven by R16D01-Gal4. mIFP was coexpressed with Drpr and thus the mIFP intensity is correlated with the Gal4 activity. Yellow dash outlines: Drpr OE region.

(B) Quantification of Orion-GFP binding on epidermal cells with or without Drpr OE. n = number of measurements: without Drpr OE (n = 16, 8 animals); with Drpr OE (n = 16, 8 animals). Welch's t-test.

(C) Distribution of fat body-drived OrionB-GFP with $Drpr^{\Delta Cyto}$ overexpressed in a patch of epidermal cells (labeled by mIFP). Yellow dash outlines: $Drpr^{\Delta Cyto}$ OE region.

(D) Quantification of Orion-GFP binding on epidermal cells with or without $Drpr^{\Delta Cyto}$ OE. n = number of measurements: without $Drpr^{\Delta Cyto}$ OE (n = 16, 8 animals); with $Drpr^{\Delta Cyto}$ OE (n = 14, 7 animals). Welch's t-test.

(E) Models of Orion function in mediating PS-Drpr interaction (left), interactions between Drpr and Orion-CD2-mIFP overexpressed by neurons (middle) or epidermal cells (right).

Continue in next page.

a result of Drpr OE, we also tested a truncated Drpr without the intracellular domain ($Drpr^{\Delta Cyto}$), which should be defective in intracellular signaling. Overexpression of $Drpr^{\Delta Cyto}$ also caused drastic OrionB-GFP accumulation on epidermal cells (Figure 5C-5D). These results suggest that OrionB interacts with the extracellular domain of Drpr directly, perhaps functioning as a bridging molecule between PS and Drpr.

Figure 5 legend continued.

(F-I) Partial dendritic fields of a control ddaC neuron (F), an OroinB-CD2-mIFP OE neuron (G), an OroinB-CD2-mIFP OE neuron with *drpr* KO in epidermal cells (H), and an OroinB-CD2-mIFP + ATP8A OE neuron (I).

(J-K) Quantification of debris coverage ratio (J) and dendrite length (K) at 96 hrs AEL. n = number of neurons: control (n = 10, 6 animals); *ppk-Gal4>OroinB-CD2-mIFP* (n = 17, 9 animals); *ppk-Gal4>OroinB-CD2-mIFP + shot-Cas9>gRNA-drpr* (n = 17, 9 animals); *ppk-Gal4>OroinB-CD2*-mIFP, *ATP8A* (n = 14, 7 animals). Kruskal-Wallis (One-way ANOVA on ranks) and Dunn's test, p-values adjusted with the Benjamini-Hochberg method.

(L) Partial dendritic field of an injured ddaC neuron at 25 hrs AI with OroinB-CD2-mIFP expressed in all epidermal cells.

(M-M") Partial dendritic field of an injured ddaC neuron at 9 hrs AI when OroinB-GFP was expressed in fat body and *ATP8A* was knocked out in *hh*-epidermal cells.

(N) Quantification of debris spread index of injured dendrites. n = number of neurons: control (n = 18, 10 animals); *R38F11>OroinB-CD2-mIFP* (n = 16, 8 animals); *Dcg-Gal4>OrionB* (n = 14, 8 animals); *Dcg-Gal4>OrionB + hh-Cas9>ATP8A* (n = 13, 8 animals). Welch's t-test.

Neurons were labeled by *ppk-MApHS* (F-I), and *ppk-CD4-tdTom* (L and M-M"). For all image panels, scale bars, 25 µm. For all quantifications, *p≤0.05, **p≤0.01, ***p≤0.001; n.s., not significant. The significance level above each genotype is for comparison with the control. Black bar, mean; red bar, SD. See also Figure S5.

348 To further test this hypothesis, we asked whether expression of an Orion that is
349 permanently tethered to the surface of otherwise wildtype dendrites could bypass the requirement
350 of PS exposure and induce Drpr-dependent phagocytosis. For this purpose, we made an OrionB-
351 CD2-mIFP (mIFP: monomeric infrared fluorescent protein; (Yu et al., 2015)) transgene in which
352 Orion is located on the extracellular side of the CD2 transmembrane domain (Yan et al., 2009).
353 As expected, overexpression of OrionB-CD2-mIFP in neurons caused robust dendrite

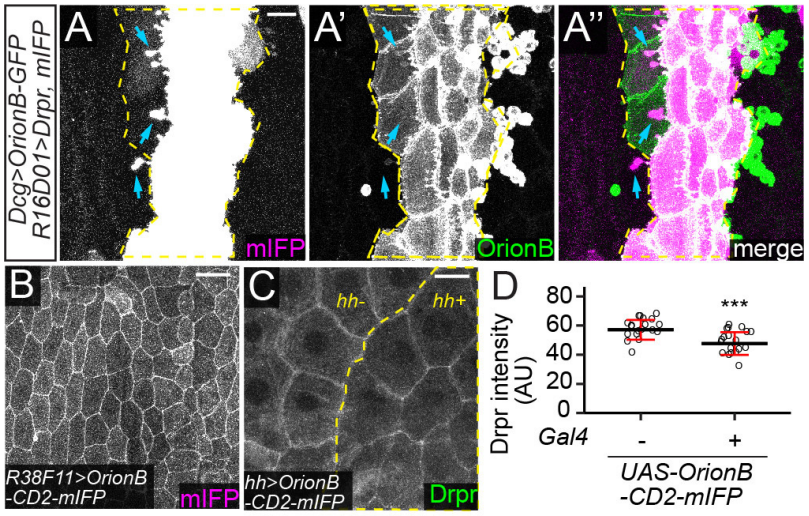

Figure S5: Orion mediates the interaction between PS and Drpr

(A-A") Protrusions (blue arrows) extended from Drpr OE epidermal cells (labeled by mIFP) in the presence of fat body-derived OrionB-GFP. Yellow dash outlines: Drpr OE region.

(B) OrionB-CD2-mIFP localization in epidermal cells driven by *R38F11-Gal4*.

(C) Drpr localization in epidermal cells with OrionB-CD2-mIFP expressed in the *hh* domain. Yellow dash outlines: *hh-Gal4>OrionB-CD2-mIFP* region.

(D) Quantification of stained Drpr levels in epidermal cells with or without OrionB-CD2-mIFP OE. n = number of measurements: w/o OrionB-CD2-mIFP OE (n = 19); w/ OrionB-CD2-mIFP OE (n = 19). Welch's t-test; ***p≤0.001; black bar, mean; red bars, SD.

Scale bars, 25 µm (A-A" and C), 50 µm (B).

354 degeneration (Figures 5E-5G, and 5J-5K). We found that this degeneration was completely
355 suppressed by epidermis-specific KO of *drpr* (Figures 5H, and 5J-5K) but was unaffected by
356 suppressing PS exposure in neurons via ATP8A OE (Figures 5I-5K). These data suggest that
357 membrane-tethered Orion is sufficient to induce PS-independent and Drpr-dependent
358 phagocytosis.

359 Meanwhile, if Orion mediates the recognition of PS by Drpr, we predict that excessive
360 Orion on the surface of epidermal cells would interact with Drpr on the same membrane and
361 interfere with the sensing of PS on dendrites. We first tested this idea by overexpressing OrionB-
362 CD2-mIFP in all epidermal cells (Figure 5E). Indeed, this manipulation fully blocked the
363 engulfment of injured dendrites at 25 hrs AI (Figures 5L and 5N). Drpr was robustly detected on
364 the cell membranes of OrionB-CD2-mIFP-expressing cells (Figures S5C and S5D), suggesting
365 that the impaired engulfment was not due to defects in Drpr subcellular localization. We then
366 tested whether accumulation of secreted Orion on the surface of epidermal cells has a similar
367 effect in blocking engulfment. Consistent with the idea that Orion binds PS, *ATP8A* KO in
368 epidermal cells resulted in a drastically increased surface level of OrionB-GFP (Figure 5M').
369 This OrionB-GFP accumulation was associated with phagocytosis deficiency, as indicated by the
370 lack of spread of dendritic debris at 9 hrs AI specifically in the *ATP8A* KO cells (Figure 5M-5N).

371 Together, our results show that interactions between Orion and Drpr from the same
372 versus apposing membranes produce opposite phenotypes (defective versus dominant dendrite
373 engulfment, respectively) and support the idea that Orion functionally bridges PS and Drpr.

374 **The Orion dosage determines the sensitivity of epidermal cells to PS-exposing dendrites**

375 While examining the phenotypes of the *orion*^{1} mutant, we noticed impaired phagocytosis in
376 *orion*^{1}/+ heterozygous larvae: Neurons with *CDC50* KO and TMEM16F OE showed no signs of
377 membrane loss or degeneration in these animals (Figures 6A, 6I, and 6J), comparable to those in
378 *orion*^{1} hemizygotes. *orion*^{1}/+ larvae also exhibited considerable suppression of *Nmnat* KO-
379 induced dendrite degeneration, albeit not to the level of *orion*^{1} hemizygotes (Figures 6B, 6I, and
380 6J). However, the engulfment of injured dendrites was normal in *orion*^{1}/+ (Figures S6A-S6B).
381 Considering that *CDC50* KO and TMEM16F OE causes milder PS exposure than does injury
382 (Sapar et al., 2018), these data suggest that removing half the dosage of Orion reduces the
383 sensitivity of epidermal cells to PS exposure on dendrites but does not block phagocytosis when

384 PS exposure is high. To further test if the Orion dosage determines the ability of epidermal cells
385 to sense PS-exposing dendrites, we increased the Orion dosage by adding an *orion* duplication to
386 the wildtype. The *orion* duplication strongly enhanced the debris level and dendrite loss in a
387 *CDC50* KO background (Figures 6D, 6I, and 6J), which by itself only causes weak PS exposure

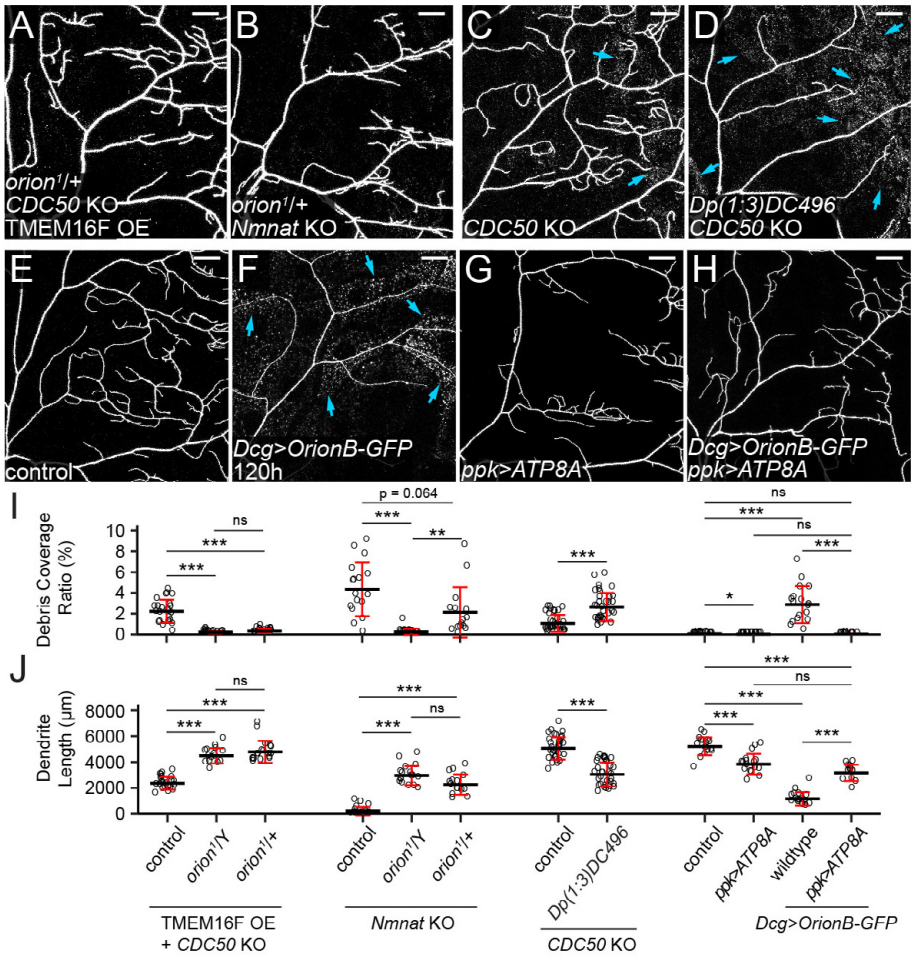

Figure 6: The Orion dosage determines the sensitivity of epidermal cells to PS-exposing dendrites

(A-B) Partial dendritic fields of a TMEM16F OE + *CDC50* KO ddaC neuron (A) and a *Nmnat* KO ddaC neuron (B) in the *orion*[1] heterozygous background.

(C-D) Partial dendritic fields of *CDC50* KO neurons in the control (C) and Dp(1;3)DC496 (D) at 120 hrs AEL. Blue arrows: debris shed from dendrites.

(E-H) Partial dendritic fields of ddaC neurons in the control (E), with fat body-derived OrionB-GFP (F), with ATP8A OE in the neuron (G), and with fat body-derived OrionB-GFP and ATP8A OE in the neuron (H) at 120 hrs AEL.

(I-L) Quantification of debris coverage ratio (I) and dendrite length (L). n = number of neurons: for TMEM16F OE + *CDC50* KO, control and *orion*[1]/Y (same dataset as in Figure 1G), *orion*[1]/+ (n = 18, 9 animals); for (I), Kruskal-Wallis (One-way ANOVA on ranks) and Dunn's test, p-values adjusted with the Benjamini-Hochberg method; for (L), one-way ANOVA and Tukey's test. For *Nmnat* KO, control and *orion*[1]/Y (same dataset as in Figure 1K), *orion*[1]/+ (n = 15, 9 animals); Kruskal-Wallis (One-way ANOVA on ranks) and Dunn's test, p-values adjusted with the Benjamini-Hochberg method. For *CDC50* KO, control (n = 33, 17 animals), Dp(1;3)DC496 (n = 33, 17 animals), Welch's t-test. For effects of *Dcg>OrionB-GFP* and *ppk>ATP8A* at 120 hrs AEL, control (n = 17, 9 animals), *ppk>ATP8A* (n = 17, 9 animals), *Dcg>OrionB-GFP* (n = 17, 9 animals), *ppk>ATP8A + Dcg>OrionB-GFP* (n = 12, 7 animals); for (I), Kruskal-Wallis (One-way ANOVA on ranks) and Dunn's test, p-values adjusted with the Benjamini-Hochberg method; for (L), one-way ANOVA and Tukey's test.

Neurons were labeled by *ppk-MApHS* (A-B and G), *ppk-CD4-tdTom* (C-F), and *ppk-Gal4>CD4-tdTom* (H). For all image panels, scale bars, 25 µm. For all quantifications, *p≤0.05, **p≤0.01, ***p≤0.001; n.s., not significant. The significance level above each genotype is for comparison with the control. Black bar, mean; red bars, SD. See also Figure S6.

388 (Sapar et al., 2018) and low levels of debris (Figures 6D, 6I, and 6J). Thus, extra Orion can
389 indeed increase the sensitivity of epidermal cells to neuronal PS.

390 Further supporting this notion, we found that fat body-derived OrionB bound to wildtype
391 dendrites at 120 hrs AEL (Figures S6C) and induced pronounced degeneration (Figures 6E, 6F,
392 and 6I-6J). This degeneration is PS-dependent because it was completely suppressed by ATP8A
393 OE in neurons (Figure 6F-6H, and 6I-6J). This surprising result demonstrates that, in late larval
394 stages, wildtype dendrites expose low levels of PS that cannot be detected by common PS
395 sensors such as AV and LactC1C2, but can be bound by overexpressed Orion.

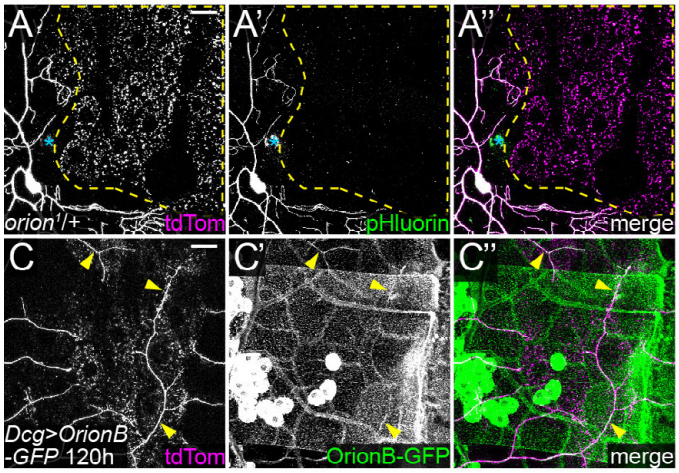

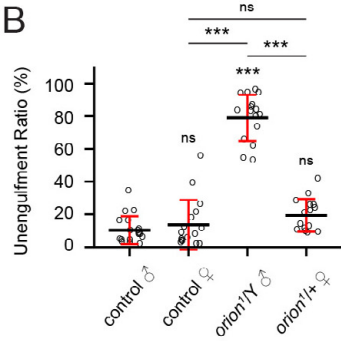

Figure S6: The Orion dosage determines the sensitivity of epidermal cells to PS-exposing dendrites

(A-A") Partial dendritic fields of a ddaC neuron in an *orion*^{1} heterozygous larva at 22 hrs AI. Yellow dash outlines: territories originally covered by injured dendrites; blue asterisks: injury sites.

(B) Quantification of unengulfment ratio of injured dendrites. n = number of neurons: control males, control females, and *orion*^{1}/Y (same dataset as in Figure 1D); *orion*^{1}/+ (n = 15, 8 animals). One-way ANOVA and Tukey's test; ***p≤0.001; n.s., not significant. The significance level above each genotype is for comparison with the control. Black bar, mean; red bars, SD.

(C-C") Partial dendritic fields of a wildtype neuron with OrionB-GFP OE in the fat body at 120 hrs AEL. Yellow arrowheads: OrionB-GFP colocalizing with dendrites.

Neurons were labeled by *ppk-MApHS* (A-A"), and *ppk-CD4-tdTom* (C-C"). For all image panels, scale bars, 25 µm.

396 **CX_3C and RRY motifs are important for Orion secretion and binding to PS**

397 Orion shares a CX_3C motif with the human chemokine CX3CL1 and an RRY motif with several
398 human neutrophil peptides. The CX_3C motif is required for Orion's function in MB remodeling
399 (Boulanger et al., 2021), but the importance of the RRY motif in Orion has not been investigated.
400 Structural prediction of OrionB by AlphaFold2 (Jumper et al., 2021) suggests that both motifs
401 are on or near the surface of the protein (Figure S7A-S7C). To test whether these motifs play any
402 role in PS-mediated dendrite engulfment, we generated *UAS-OrionB-GFP* variants carrying

403 mutations in them (OrionB^{AX3C} and OrionB^{AAY}). In addition, to understand how the G611D point

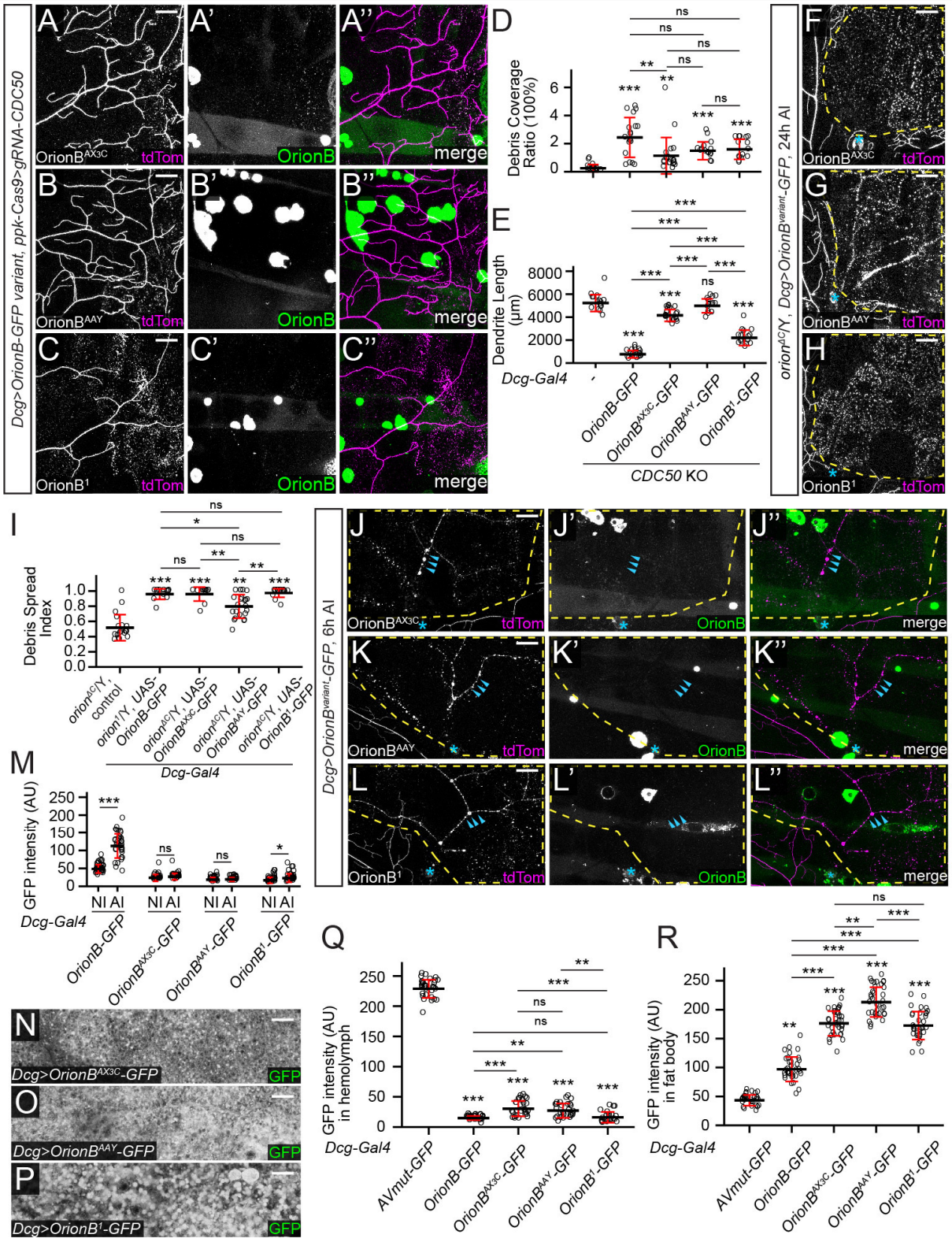

Figure 7: CX$_3$C and RRY motifs are important for Orion secretion and binding to PS

Continue in next page.

Figure 7 legend continued.

(A-C") Partial dendritic fields of *CDC5O* KO ddaC neurons with OrionB^{AX3C}-GFP (A-A"), OrionB^{AAY}-GFP (B-B"), and OrionB^{1}-GFP (C-C") expressed in the fat body at 120 hrs AEL.

(D-E) Quantification of debris coverage ratio (D) and dendrite length (E) at 120 hrs AEL. n = number of neurons: *CDC50* KO control (n = 16, 8 animals); *CDC50* KO + *Dcg>OrionB-GFP* (n = 18, 9 animals); *CDC50* KO + *Dcg>OrionB^{AX3C}-GFP* (n = 20, 10 animals); *CDC50* KO + *Dcg>OrionB^{AAY}-GFP* (n = 16, 8 animals); *CDC50* KO + *Dcg>OrionB^{1}-GFP* (n = 15, 8 animals). For (D), Kruskal-Wallis (One-way ANOVA on ranks) and Dunn's test, p-values adjusted with the Benjamini-Hochberg method; for (E), one-way ANOVA and Tukey's test.

(F) Partial dendritic fields of ddaC neurons in *orion$^{\Delta C}$* hemizygous larvae with OrionB^{AX3C}-GFP (F), OrionB^{AAY}-GFP (G), and OrionB^{1}-GFP (H) expressed by the fat body at 22-24 hrs AI. Yellow dash outlines: territories originally covered by injured dendrites; blue asterisks: injury sites.

(I) Quantification of debris spread index of injured dendrites. n = number of neurons: *orion$^{\Delta C}$*/Y control (n = 19, 9 animals); *orion^{1}*/Y + *Dcg>OrionB-GFP* (same dataset as in 2M); *orion$^{\Delta C}$*/Y + *Dcg>OrionB^{AX3C}-GFP* (n = 12, 7 animals); *orion$^{\Delta C}$*/Y + *Dcg>OrionB^{AAY}-GFP* (n = 23, 12 animals); *orion$^{\Delta C}$*/Y + *Dcg>OrionB^{1}-GFP* (n = 15, 8 animals). Kruskal-Wallis (One-way ANOVA on ranks) and Dunn's test, p-values adjusted with the Benjamini-Hochberg method.

(J-L") OrionB^{variant}-GFP distribution on injured ddaC dendrites with OrionB^{AX3C}-GFP (J-J"), OrionB^{AAY}-GFP (K-K"), and OrionB^{1}-GFP (L-L") expressed by the fat body at 6 hrs AI. Yellow dash outlines: territories originally covered by injured dendrites; blue asterisks: injury sites; blue arrowheads: injured dendrite fragments lacking GFP labeling.

(M) Quantification of GFP binding on injured dendrites. n = number of measurements: *Dcg>OrionB-GFP* NI and AI (same dataset as in 3D); *Dcg>OrionB^{AX3C}-GFP* NI (n = 24, 8 animals); *Dcg>OrionB^{AX3C}-GFP* AI (n = 26, 8 animals); *Dcg>OrionB^{AAY}-GFP* NI (n = 26, 9 animals); *Dcg>OrionB^{AAY}-GFP* AI (n = 27, 9 animals); *Dcg>OrionB^{1}-GFP* NI (n = 36, 9 animals); *Dcg>OrionB^{1}-GFP* AI (n = 36, 9 animals).Welch's t-test.

(N-P) GFP levels in fat bodies expressing OrionB^{AX3C}-GFP (N), OrionB^{AAY}-GFP (O), and OrionB^{1}-GFP (P) at 120 hrs AEL.

(Q) Quantification of GFP levels in hemolymph. AVmut-GFP (Sapar et al., 2018) is a control for maximal secretion. n = number of measurements: *Dcg>AVmut-GFP* (n = 31, 8 animals); *Dcg>OrionB-GFP* (n = 28, 7 animals); *Dcg>OrionB^{AX3C}-GFP* (n = 28, 7 animals); *Dcg>OrionB^{AAY}-GFP* (n = 27, 7 animals); *Dcg>OrionB^{1}-GFP* (n = 22, 7 animals). Kruskal-Wallis (One-way ANOVA on ranks) and Dunn's test, p-values adjusted with the Benjamini-Hochberg method.

(R) Quantification of GFP levels in the fat body. n = number of measurements: *Dcg>AVmut-GFP* (n = 31, 8 animals); *Dcg>OrionB-GFP* (n = 34, 9 animals); *Dcg>OrionB^{AX3C}-GFP* (n = 35, 9 animals); *Dcg>OrionB^{AAY}-GFP* (n = 36, 9 animals); *Dcg>OrionB^{1}-GFP* (n = 34, 9 animals). Kruskal-Wallis (One-way ANOVA on ranks) and Dunn's test, p-values adjusted with the Benjamini-Hochberg method.

Neurons were labeled by *ppk-CD4-tdTom* (A-C", F-H, and J-L"). For all image panels, scale bars, 25 μm. For all quantifications, *p≤0.05, **p≤0.01, ***p≤0.001; n.s., not significant. The significance level above each genotype is for comparison with the control. Black bar, mean; red bars, SD. See also Figure S7.

mutation in *orion^{1}* affects Orion function, we also made *UAS-OrionB^{1}-GFP*. We first compared these OrionB-GFP variants in their abilities to potentiate dendrite degeneration of *CDC50* KO neurons. Fat body-derived OrionB^{AX3C}, OrionB^{AAY}, and OrionB^{1} all potentiated the debris level of *CDC50* KO neurons (Figures 7A-7D). They also induced various degrees of dendrite reduction as compared to *CDC50* KO alone, with OrionB^{1} being the most potent and OrionB^{AAY} the least (Figures 7A-7E). However, their effects on dendrite reduction are much weaker (5%-58% reduction) than that of the wildtype OrionB-GFP (85% reduction) (Figures 7D and 7E). We

next tested OrionB-GFP variants in rescuing *orion*$^{\Delta C}$ hemizygotes with the dendrite injury assay. All but OrionB^{AAY} restored the engulfment of injured dendrites to the same level as the wildtype OrionB (Figures 7F-7I). These results suggest that these mutations impair, but do not abolish, Orion activity. Among the mutant variants, Orion^{1} seems to have the highest activity whereas OrionB^{AAY} seems to be the least active.

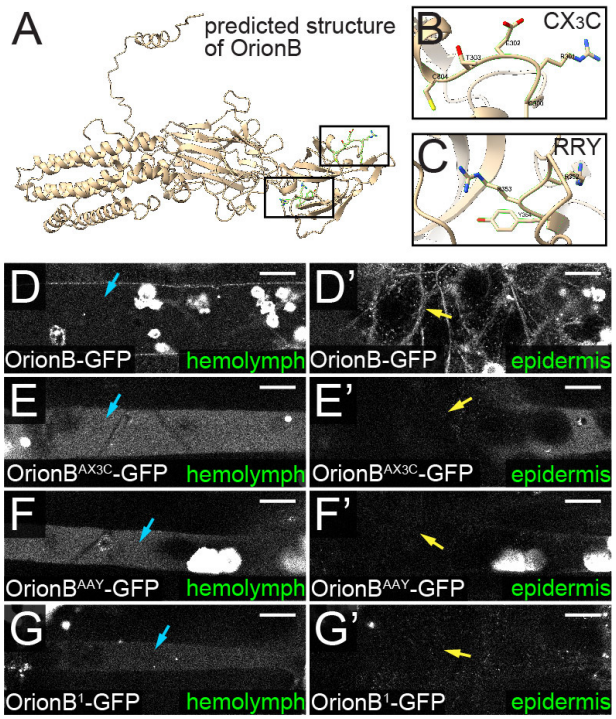

Figure S7: CX$_3$C and RRY motifs are important for Orion secretion and binding to PS

(A-C) Structure prediction of OrionB (A, beige) by AlphaFold2. Close-up of putative CX$_3$C (B) and RRY (C) motifs.

(D-G") GFP levels in hemolymph (blue arrowheads) and on epidermal cells (yellow arrowheads) with OrionB-GFP (D and D'), OrionB^{AX3C}-GFP (E and E'), OrionB^{AAY}-GFP (F and F'), and OrionB^{1}-GFP (G and G') expressed by the fat body at 120 hrs AEL. Scale bars, 25 µm.

To further determine whether the mutations affect OrionB activity by interfering with its PS-interaction, we examined the binding of OrionB variants on injured dendrites. Whereas WT OrionB-GFP bound to fragmenting dendrites robustly (Figures 3C-3D), none of the mutant variants showed obvious binding (Figures 7J-7M), except that OrionB^{1}-GFP showed occasional colocalization with large pieces of debris. The lack of binding was not due to absence of extracellular OrionB-GFP proteins, as mutant variants showed similar (for OrionB^{1}-GFP) or higher (for OrionB^{AX3C} and OrionB^{AAY}) hemolymph levels as compared to the wildtype OrionB-GFP (Figures S7D, S7E, S7F, S7G, and 7Q). These results suggest that the mutant variants have impaired abilities to bind PS on injured dendrites. In addition, distinct from the wildtype OrionB-GFP (Figure S7D'), the mutant variants did not show obvious binding on the surface of peripheral tissues (Figures S7E', S7F, and S7G').

Lastly, we noticed that all OrionB-GFP mutants were present at higher levels in the fat body than the WT version, with OrionB^{AAY} showing the highest level (Figures 7N-7P, and 7R).

429 Considering that all *UAS-OrionB-GFP* transgenes are identical except for the mutations, and
430 thus should be expressed at comparable levels, these data suggest that these mutations
431 additionally reduce protein secretion from the fat body into the hemolymph.

432 Together, above results revealed that the CX_3C and RRY motifs, as well as G611, are
433 important for the secretion of Orion and for its binding to PS.

434 **DISCUSSION**

435 **Orion functions as a bridging molecule between PS and Drpr**

436 By triggering phagocytosis, the recognition of PS exposed on neurons is a critical event during
437 neurodegeneration and clearance. Although several studies have implied the involvement of Drpr
438 in this process in *Drosophila* (Awasaki et al., 2006; Freeman et al., 2003; Han et al., 2014; Ji et
439 al., 2022; MacDonald et al., 2006; Sapar et al., 2018; Williams et al., 2006), how Drpr mediates
440 PS recognition is unclear. Because the extracellular domain of Drpr can directly interact with PS
441 (Tung et al., 2013), Drpr has been considered as a PS receptor (Williamson and Vale, 2018). In
442 this study, we present several lines of *in vivo* evidence that strongly suggest the *Drosophila*
443 chemokine-like Orion is a PS-binding bridging molecule that enables Drpr to respond to
444 neuronal PS exposure. First, Orion is required for all scenarios of Drpr-dependent phagocytosis
445 of sensory dendrites and functions upstream of Drpr. Second, Orion binds to PS on the cell
446 surface. We show that Orion binds to neurons and epidermal cells that expose PS as a result of
447 tissue-specific KO of the PS flippase ATP8A. In addition, ATP8A OE, which retains PS in the
448 inner membrane leaflet, eliminates Orion binding on healthy dendrites and epidermal cells,
449 suggesting that this binding is PS-dependent. Importantly, Orion outcompetes Annexin V for
450 binding to injured dendrites, suggesting that Orion directly interacts with PS. Third, when
451 overexpressed, both full-length and intracellular domain-lacking Drpr proteins can trap Orion on
452 the cell surface, suggesting that Drpr interacts with Orion through Drpr's extracellular domain.
453 Lastly, when expressed in neurons, membrane-tethered Orion bypasses the requirement for PS in
454 inducing Drpr-dependent engulfment, but when expressed in phagocytes, membrane-tethered
455 Orion blocks PS-induced engulfment. These observations all point to Orion as a functional link
456 between PS and Drpr.

457 Previously, SIMU, a PS-binding transmembrane protein expressed by *Drosophila*
458 embryonic phagocytes, was originally proposed to be a bridging molecule (Kurant et al., 2008).
459 However, Orion and SIMU contribute to phagocytosis through distinct mechanisms. First, SIMU
460 is expressed by phagocytes to allow them to tether apoptotic cells (Kurant et al., 2008), while
461 Orion is secreted from many peripheral tissues and functions as an opsonin to enable
462 phagocytosis. Second, SIMU is a membrane protein that shares homology with Drpr but
463 functions at a different step in apoptotic neuron clearance compared to Drpr (Kurant et al., 2008).
464 In contrast, as a secreted protein, Orion interacts with Drpr and functions at the same step of
465 phagocytosis as Drpr. Therefore, SIMU behaves more like a tethering receptor (Shklyar et al.,
466 2013), while Orion represents a true PS-bridging molecule in *Drosophila* and is functionally
467 analogous to other PS-bridging molecules in mammals and worms. Although we focus our
468 analyses on the engulfment of somatosensory dendrites, the ubiquitous roles of PS and Drpr in
469 phagocytosis and the broad expression patterns of Orion suggest that Orion may be widely
470 involved in PS-mediated phagocytosis in *Drosophila*. This view is supported by our findings that
471 Orion deposited in the hemolymph can mediate phagocytosis in distant tissues and that the
472 accumulation of Orion on epidermal cells turns these cells into targets of phagocytosis.

473 **The level of Orion modulates phagocyte sensitivity to PS**

474 Although the role of PS exposure in inducing phagocytosis has been well documented (Lemke,
475 2019; Nagata, 2018), what determines the sensitivity of phagocytes to PS is much less
476 understood. In this study, we discovered that the available level of secreted PS-bridging
477 molecules is a determinant of phagocyte sensitivity to PS. We show that reducing the dosage of
478 functional Orion by one half makes phagocytes blind to dendrites with moderate levels of PS
479 exposure (i.e. *CDC50* KO + TMEME16F OE neurons and *Nmnat* KO neurons), but the reduced
480 Orion does not affect the ability of phagocytes to engulf dendrites that display high levels of PS
481 exposure (i.e. injury). Conversely, an extra copy of the *orion* locus enhances the ability of
482 phagocytes to engulf dendrites that have mild PS exposure (i.e. *CDC50* KO). These results
483 suggest that endogenous Orion is likely expressed at a balanced level to enable the right amount
484 of phagocytosis: Too much Orion may cause unintended phagocytosis of stressed cells that
485 display mild PS exposure, while too little Orion may interfere with efficient clearance of sick
486 cells or structures that are beyond rescue. Consistent with this idea, endogenous Orion is
487 expressed at a low level during larval development (Figure S2F and S2H), but is dramatically

488 upregulated during metamorphosis (Boulanger et al., 2021), a time when large-scale tissue
489 remodeling and clearance take place (Williams and Truman, 2005b).

490 **Orion has distinct roles in neurite maintenance and remodeling**

491 Orion was previously known to be required for axonal pruning and clearance of MB γ neurons
492 during metamorphosis (Boulanger et al., 2021). In that context, Orion is expressed in the
493 remodeling MB neurons and functions as a "find-me" signal for glia to penetrate the axon
494 bundles and engulf axonal debris. In contrast, in the larval peripheral nervous system (PNS),
495 Orion is supplied by many non-neural tissues and functions as a permissive signal for
496 phagocytosis of sick or broken dendrites. This distinction is likely due to two differences
497 between the larval PNS and the remodeling CNS. First, in the PNS, the dendrites of da neurons
498 are exposed to the hemolymph and are readily accessible to Orion that is secreted from other
499 tissues, whereas in the CNS, the axons are more tightly packed and may be harder for extrinsic
500 Orion to access. Neuron-derived Orion would thus be more effective than extrinsic Orion for
501 promoting phagocytosis in the CNS. Intriguingly, we detected Orion expression in a small
502 number of neurons in the larval ventral nerve cord (VNC). It will be interesting to find out
503 whether these neurons are particularly subject to degeneration. Second, compared to the larval
504 PNS where degenerative events are rare, the nervous system undergoing metamorphosis has a
505 much greater demand for phagocytosis. Turning on Orion expression in neurons may thus be
506 required for efficient clearance of all pruned neurites. Consistent with this idea, we detected
507 Orion expression also in a subset of da neurons during metamorphosis.

508 **Orion possesses unique properties compared to other PS-binding molecules**

509 Fluorescent PS probes based on AV and Lact are widely used to visualize PS exposure in cell
510 culture and live animals and have been crucial for many discoveries in PS biology (Andersen et
511 al., 2000; Hanayama et al., 2002; Koopman et al., 1994; Mapes et al., 2012; Sapar et al., 2018).
512 LactC1C2 is known to have a higher affinity to PS than AV (Andree et al., 1990; Shi et al., 2004;
513 Tait and Gibson, 1992). We previously observed additional differences between these two
514 proteins. Compared to LactC1C2, which coats the dendrite surface well, AV tends to traffic to
515 endocytic vesicles inside PS-exposing dendrites, consistent with the ability of the AV complex to
516 induce endocytosis upon PS-binding (Kenis et al., 2004; Oling et al., 2000). Importantly, unlike
517 AV, which does not alter the kinetics of neurite degeneration, LactC1C2 binding to PS-exposing

518 dendrites potentiates Drpr-dependent degeneration (Sapar et al., 2018). This latter observation
519 previously led us to hypothesize that LactC1C2 may contain unknown sequences that interact
520 with Drpr (Sapar et al., 2018). In this study, we show that the effect of LactC1C2 in exacerbating
521 dendrite degeneration depends on Orion, suggesting instead that LactC1C2 may indirectly
522 promote phagocyte/dendrite interactions by enhancing Orion function. One possible mechanism
523 is that LactC1C2 binding on the plasma membrane further disrupts the membrane and causes
524 more PS exposure that can subsequently be detected by endogenous Orion.

525 Compared to AV and LactC1C2, Orion displays unique *in vivo* binding properties.
526 Notably, our evidence suggests that Orion may have the highest affinity for PS among the three.
527 First, it efficiently outcompetes AV in binding to injured dendrites. Second, overexpressed Orion
528 shows PS-dependent binding to healthy epidermal cells and dendrites (albeit the latter only in
529 wandering 3rd instar larvae), while AV and LactC1C2 do not (Sapar et al., 2018). Although we
530 cannot rule out the possibility that Orion also binds other molecules on the cell membrane in a
531 PS-dependent manner, further characterization of the PS-binding domain of Orion may result in
532 novel and exquisitely sensitive PS sensors.

533 The surprising finding that overexpressed Orion binds to peripheral tissues and dendrites
534 suggest that these cells expose PS under physiological conditions, perhaps at a level too low to
535 detect by AV and LactC1C2. Thus, low levels of PS exposure may be much more prevalent *in*
536 *vivo* than previously thought. Intriguingly, binding of overexpressed Orion induces degeneration
537 of wildtype dendrites but does not cause obvious phagocytosis of other non-neural tissues,
538 suggesting that neurons may be more vulnerable to PS-induced phagocytosis than other cell
539 types.

540 **Functional conservation between Orion and human immunomodulatory proteins**

541 Recently, many human chemokines were found to bind to PS exposed on apoptotic vesicles and
542 serve as "find-me" signals to attract phagocytes (Pontejo and Murphy, 2021). Orion shares the
543 CX_3C motif with the mammalian chemokine CXC3L1 and has also three glycosaminoglycan
544 (GAG) putative binding sequences, a hallmark of chemokine activity (Monneau et al., 2016).
545 Even though direct binding to PS has not been demonstrated for CXC3L1, this chemokine is
546 required for microglia-mediated synapse elimination after whisker lesioning (Gunner et al.,
547 2019), a process likely involving PS exposure (Faust et al., 2021). In addition, Orion contains a

548 RRY motif commonly found in human neutrophil peptides, small antimicrobial peptides
549 important for innate immunity (Klotman and Chang, 2006). We found that both CX_3C and RRY
550 motifs are important for Orion function, likely by affecting Orion secretion and PS-binding.
551 Although Orion does not show global sequence homologies to mammalian immunomodulatory
552 proteins, its interaction partner Drpr has mammalian homologs that are involved in phagocytosis
553 of neurons through unknown mechanisms (Wu et al., 2009). Thus, the common features between
554 Orion and human proteins indicate that a functional conservation may exist between PS-sensing
555 mechanisms in insects and humans.

556 **METHODS**

557 **Fly strains**

558 The details of fly strains used in this study are listed in Table S1 (Key Resource Table). For
559 labeling of C4da neurons, we used *ppk-MApHS*, *ppk-CD4-tdTom*, and *ppk-Gal4 UAS-CD4-*
560 *tdTom*. For labeling of all da neurons, we used *21-7-Gal4 UAS-CD4-tdTom*. For labeling PS
561 exposure on dendrites, we used *dcg-Gal4 UAS-AnnexinV-mCard* and *dcg-Gal4 UAS-GFP-*
562 *LactC1C2*. For visualizing OrionB labeling on cell surface, we used *dcg-Gal4 UAS-OrionB-*
563 *GFP*, *Dcg-LexA LexAop-OrionB-GFP*, and *R16A03-LexA LexAop-OrionB-GFP*. We generated
564 *dcg-LexA* by converting the Gal4 in *dcg-Gal4* into LexAGAD. The conversion process will be
565 published elsewhere.

566 See Supplemental Methods for details of molecular cloning and transgenic flies,
567 generation of KI flies, CRISPR-TRiM, live imaging, immunohistochemistry, image analysis and
568 quantification, and statistical analysis. See Table S2 for gRNA target sequences.

569 **ACKNOWLEDGMENTS**

570 We thank Larry Zipursky, Loren Looger, Xinhua Lin, BACPAC Resources Center, *Drosophila*
571 Genomics Resource Center (DGRC), the National Cancer Institute (NCI), and Addgene for
572 plasmids; Marc Freeman and Bloomington Stock Center for fly stocks; Cornell BRC Imaging
573 facility for access to microscopes (funded by NIH grant S10OD018516); Cornell CSCU for
574 advice on statistics; Mike Goldberg for critical reading and suggestions on the manuscript. This
575 work was supported by NIH grants (R01NS099125 and R21OD023824) awarded to C.H., and by
576 ARC grant (PJA 20151203422) and FRM grant (DEQ20160334870) awarded to J.-M.D.

DECLARATION OF INTEREST

The authors declare no competing interests.

579 **REFERENCE**

580 Andersen, M.H., Graversen, H., Fedosov, S.N., Petersen, T.E., and Rasmussen, J.T. (2000).
581 Functional analyses of two cellular binding domains of bovine lactadherin. Biochemistry *39*,
582 6200-6206.
583 Andree, H.A., Reutelingsperger, C.P., Hauptmann, R., Hemker, H.C., Hermens, W.T., and
584 Willems, G.M. (1990). Binding of vascular anticoagulant alpha (VAC alpha) to planar
585 phospholipid bilayers. J Biol Chem *265*, 4923-4928.
586 Awasaki, T., Tatsumi, R., Takahashi, K., Arai, K., Nakanishi, Y., Ueda, R., and Ito, K. (2006).
587 Essential role of the apoptotic cell engulfment genes draper and ced-6 in programmed axon
588 pruning during Drosophila metamorphosis. Neuron *50*, 855-867.
589 Bazan, J.F., Bacon, K.B., Hardiman, G., Wang, W., Soo, K., Rossi, D., Greaves, D.R., Zlotnik, A.,
590 and Schall, T.J. (1997). A new class of membrane-bound chemokine with a CX3C motif. Nature
591 *385*, 640-644.
592 Bevers, E.M., and Williamson, P.L. (2016). Getting to the Outer Leaflet: Physiology of
593 Phosphatidylserine Exposure at the Plasma Membrane. Physiol Rev *96*, 605-645.
594 Botelho, R.J., and Grinstein, S. (2011). Phagocytosis. Curr Biol *21*, R533-538.
595 Boulanger, A., Thinat, C., Zuchner, S., Fradkin, L.G., Lortat-Jacob, H., and Dura, J.M. (2021).
596 Axonal chemokine-like Orion induces astrocyte infiltration and engulfment during mushroom
597 body neuronal remodeling. Nat Commun *12*, 1849.
598 Chen, Y., Akin, O., Nern, A., Tsui, C.Y., Pecot, M.Y., and Zipursky, S.L. (2014). Cell-type-specific
599 labeling of synapses in vivo through synaptic tagging with recombination. Neuron *81*, 280-293.
600 Chung, W.S., Clarke, L.E., Wang, G.X., Stafford, B.K., Sher, A., Chakraborty, C., Joung, J., Foo,
601 L.C., Thompson, A., Chen, C.*, et al.* (2013). Astrocytes mediate synapse elimination through
602 MEGF10 and MERTK pathways. Nature *504*, 394-400.
603 Darland-Ransom, M., Wang, X., Sun, C.L., Mapes, J., Gengyo-Ando, K., Mitani, S., and Xue, D.
604 (2008). Role of C. elegans TAT-1 protein in maintaining plasma membrane phosphatidylserine
605 asymmetry. Science *320*, 528-531.
606 Faust, T.E., Gunner, G., and Schafer, D.P. (2021). Mechanisms governing activity-dependent
607 synaptic pruning in the developing mammalian CNS. Nat Rev Neurosci *22*, 657-673.

608 Feng, S., Sekine, S., Pessino, V., Li, H., Leonetti, M.D., and Huang, B. (2017). Improved split
609 fluorescent proteins for endogenous protein labeling. Nat Commun *8*, 370.
610 Fourgeaud, L., Traves, P.G., Tufail, Y., Leal-Bailey, H., Lew, E.D., Burrola, P.G., Callaway, P.,
611 Zagorska, A., Rothlin, C.V., Nimmerjahn, A.*, et al.* (2016). TAM receptors regulate multiple
612 features of microglial physiology. Nature *532*, 240-244.
613 Freeman, M.R., Delrow, J., Kim, J., Johnson, E., and Doe, C.Q. (2003). Unwrapping glial biology:
614 Gcm target genes regulating glial development, diversification, and function. Neuron *38*, 567-
615 580.
616 Frost, J.L., and Schafer, D.P. (2016). Microglia: Architects of the Developing Nervous System.
617 Trends Cell Biol *26*, 587-597.
618 Fuentes-Medel, Y., Logan, M.A., Ashley, J., Ataman, B., Budnik, V., and Freeman, M.R. (2009).
619 Glia and muscle sculpt neuromuscular arbors by engulfing destabilized synaptic boutons and
620 shed presynaptic debris. PLoS Biol *7*, e1000184.
621 Galloway, D.A., Phillips, A.E.M., Owen, D.R.J., and Moore, C.S. (2019). Phagocytosis in the Brain:
622 Homeostasis and Disease. Front Immunol *10*, 790.
623 Gunner, G., Cheadle, L., Johnson, K.M., Ayata, P., Badimon, A., Mondo, E., Nagy, M.A., Liu, L.,
624 Bemiller, S.M., Kim, K.W.*, et al.* (2019). Sensory lesioning induces microglial synapse elimination
625 via ADAM10 and fractalkine signaling. Nat Neurosci *22*, 1075-1088.
626 Han, C., Song, Y., Xiao, H., Wang, D., Franc, N.C., Jan, L.Y., and Jan, Y.N. (2014). Epidermal cells
627 are the primary phagocytes in the fragmentation and clearance of degenerating dendrites in
628 Drosophila. Neuron *81*, 544-560.
629 Han, C., Wang, D., Soba, P., Zhu, S., Lin, X., Jan, L.Y., and Jan, Y.N. (2012). Integrins regulate
630 repulsion-mediated dendritic patterning of drosophila sensory neurons by restricting dendrites
631 in a 2D space. Neuron *73*, 64-78.
632 Hanayama, R., Tanaka, M., Miwa, K., Shinohara, A., Iwamatsu, A., and Nagata, S. (2002).
633 Identification of a factor that links apoptotic cells to phagocytes. Nature *417*, 182-187.
634 Ji, H., and Han, C. (2020). LarvaSPA, A Method for Mounting Drosophila Larva for Long-Term
635 Time-Lapse Imaging. J Vis Exp.

636 Ji, H., Sapar, M.L., Sarkar, A., Wang, B., and Han, C. (2022). Phagocytosis and self-destruction
637 break down dendrites of Drosophila sensory neurons at distinct steps of Wallerian
638 degeneration. Proceedings of the National Academy of Sciences *119*, e2111818119.
639 Jumper, J., Evans, R., Pritzel, A., Green, T., Figurnov, M., Ronneberger, O., Tunyasuvunakool, K.,
640 Bates, R., Zidek, A., Potapenko, A.*, et al.* (2021). Highly accurate protein structure prediction
641 with AlphaFold. Nature *596*, 583-589.
642 Kenis, H., van Genderen, H., Bennaghmouch, A., Rinia, H.A., Frederik, P., Narula, J., Hofstra, L.,
643 and Reutelingsperger, C.P. (2004). Cell surface-expressed phosphatidylserine and annexin A5
644 open a novel portal of cell entry. J Biol Chem *279*, 52623-52629.
645 Klotman, M.E., and Chang, T.L. (2006). Defensins in innate antiviral immunity. Nat Rev Immunol
646 *6*, 447-456.
647 Koopman, G., Reutelingsperger, C.P., Kuijten, G.A., Keehnen, R.M., Pals, S.T., and van Oers, M.H.
648 (1994). Annexin V for flow cytometric detection of phosphatidylserine expression on B cells
649 undergoing apoptosis. Blood *84*, 1415-1420.
650 Kurant, E., Axelrod, S., Leaman, D., and Gaul, U. (2008). Six-microns-under acts upstream of
651 Draper in the glial phagocytosis of apoptotic neurons. Cell *133*, 498-509.
652 Lemke, G. (2019). How macrophages deal with death. Nat Rev Immunol *19*, 539-549.
653 Leventis, P.A., and Grinstein, S. (2010). The distribution and function of phosphatidylserine in
654 cellular membranes. Annu Rev Biophys *39*, 407-427.
655 Li, T., Chiou, B., Gilman, C.K., Luo, R., Koshi, T., Yu, D., Oak, H.C., Giera, S., Johnson-Venkatesh,
656 E., Muthukumar, A.K.*, et al.* (2020). A splicing isoform of GPR56 mediates microglial synaptic
657 refinement via phosphatidylserine binding. EMBO J *39*, e104136.
658 Ma, W., Rai, V., Hudson, B.I., Song, F., Schmidt, A.M., and Barile, G.R. (2012). RAGE binds C1q
659 and enhances C1q-mediated phagocytosis. Cell Immunol *274*, 72-82.
660 MacDonald, J.M., Beach, M.G., Porpiglia, E., Sheehan, A.E., Watts, R.J., and Freeman, M.R.
661 (2006). The Drosophila cell corpse engulfment receptor Draper mediates glial clearance of
662 severed axons. Neuron *50*, 869-881.

663 Maciejewski-Lenoir, D., Chen, S., Feng, L., Maki, R., and Bacon, K.B. (1999). Characterization of
664 fractalkine in rat brain cells: migratory and activation signals for CX3CR-1-expressing microglia. J
665 Immunol *163*, 1628-1635.
666 Mapes, J., Chen, Y.Z., Kim, A., Mitani, S., Kang, B.H., and Xue, D. (2012). CED-1, CED-7, and TTR-
667 52 regulate surface phosphatidylserine expression on apoptotic and phagocytic cells. Curr Biol
668 *22*, 1267-1275.
669 Miyanishi, M., Tada, K., Koike, M., Uchiyama, Y., Kitamura, T., and Nagata, S. (2007).
670 Identification of Tim4 as a phosphatidylserine receptor. Nature *450*, 435-439.
671 Monneau, Y., Arenzana-Seisdedos, F., and Lortat-Jacob, H. (2016). The sweet spot: how GAGs
672 help chemokines guide migrating cells. J Leukoc Biol *99*, 935-953.
673 Nagata, S. (2018). Apoptosis and Clearance of Apoptotic Cells. Annu Rev Immunol *36*, 489-517.
674 Nagata, S., Suzuki, J., Segawa, K., and Fujii, T. (2016). Exposure of phosphatidylserine on the cell
675 surface. Cell Death Differ *23*, 952-961.
676 Nandrot, E.F., Anand, M., Almeida, D., Atabai, K., Sheppard, D., and Finnemann, S.C. (2007).
677 Essential role for MFG-E8 as ligand for alphavbeta5 integrin in diurnal retinal phagocytosis. Proc
678 Natl Acad Sci U S A *104*, 12005-12010.
679 Oling, F., Santos, J.S., Govorukhina, N., Mazeres-Dubut, C., Bergsma-Schutter, W., Oostergetel,
680 G., Keegstra, W., Lambert, O., Lewit-Bentley, A., and Brisson, A. (2000). Structure of membrane-
681 bound annexin A5 trimers: a hybrid cryo-EM - X-ray crystallography study. J Mol Biol *304*, 561-
682 573.
683 Paidassi, H., Tacnet-Delorme, P., Garlatti, V., Darnault, C., Ghebrehiwet, B., Gaboriaud, C.,
684 Arlaud, G.J., and Frachet, P. (2008). C1q binds phosphatidylserine and likely acts as a
685 multiligand-bridging molecule in apoptotic cell recognition. J Immunol *180*, 2329-2338.
686 Park, D., Tosello-Trampont, A.C., Elliott, M.R., Lu, M., Haney, L.B., Ma, Z., Klibanov, A.L.,
687 Mandell, J.W., and Ravichandran, K.S. (2007). BAI1 is an engulfment receptor for apoptotic cells
688 upstream of the ELMO/Dock180/Rac module. Nature *450*, 430-434.
689 Park, J., Choi, Y., Jung, E., Lee, S.H., Sohn, J.W., and Chung, W.S. (2021). Microglial MERTK
690 eliminates phosphatidylserine-displaying inhibitory post-synapses. EMBO J *40*, e107121.

691 Poe, A.R., Wang, B., Sapar, M.L., Ji, H., Li, K., Onabajo, T., Fazliyeva, R., Gibbs, M., Qiu, Y., Hu, Y.,
692 *et al.* (2019). Robust CRISPR/Cas9-Mediated Tissue-Specific Mutagenesis Reveals Gene
693 Redundancy and Perdurance in Drosophila. Genetics *211*, 459-472.
694 Pontejo, S.M., and Murphy, P.M. (2021). Chemokines act as phosphatidylserine-bound "find-
695 me" signals in apoptotic cell clearance. PLoS Biol *19*, e3001259.
696 Port, F., Chen, H.M., Lee, T., and Bullock, S.L. (2014). Optimized CRISPR/Cas tools for efficient
697 germline and somatic genome engineering in Drosophila. Proc Natl Acad Sci U S A *111*, E2967-
698 2976.
699 Salter, M.W., and Stevens, B. (2017). Microglia emerge as central players in brain disease. Nat
700 Med *23*, 1018-1027.
701 Sapar, M.L., Ji, H., Wang, B., Poe, A.R., Dubey, K., Ren, X., Ni, J.Q., and Han, C. (2018).
702 Phosphatidylserine Externalization Results from and Causes Neurite Degeneration in
703 Drosophila. Cell Rep *24*, 2273-2286.
704 Schafer, D.P., Lehrman, E.K., Kautzman, A.G., Koyama, R., Mardinly, A.R., Yamasaki, R.,
705 Ransohoff, R.M., Greenberg, M.E., Barres, B.A., and Stevens, B. (2012). Microglia sculpt
706 postnatal neural circuits in an activity and complement-dependent manner. Neuron *74*, 691-
707 705.
708 Scott-Hewitt, N., Perrucci, F., Morini, R., Erreni, M., Mahoney, M., Witkowska, A., Carey, A.,
709 Faggiani, E., Schuetz, L.T., Mason, S.*, et al.* (2020). Local externalization of phosphatidylserine
710 mediates developmental synaptic pruning by microglia. EMBO J *39*, e105380.
711 Segawa, K., and Nagata, S. (2015). An Apoptotic 'Eat Me' Signal: Phosphatidylserine Exposure.
712 Trends Cell Biol *25*, 639-650.
713 Shacham-Silverberg, V., Sar Shalom, H., Goldner, R., Golan-Vaishenker, Y., Gurwicz, N.,
714 Gokhman, I., and Yaron, A. (2018). Phosphatidylserine is a marker for axonal debris engulfment
715 but its exposure can be decoupled from degeneration. Cell Death Dis *9*, 1116.
716 Shaner, N.C., Lambert, G.G., Chammas, A., Ni, Y., Cranfill, P.J., Baird, M.A., Sell, B.R., Allen, J.R.,
717 Day, R.N., Israelsson, M.*, et al.* (2013). A bright monomeric green fluorescent protein derived
718 from Branchiostoma lanceolatum. Nat Methods *10*, 407-409.

719 Shi, J., Heegaard, C.W., Rasmussen, J.T., and Gilbert, G.E. (2004). Lactadherin binds selectively
720 to membranes containing phosphatidyl-L-serine and increased curvature. Biochim Biophys Acta
721 *1667*, 82-90.
722 Shklyar, B., Levy-Adam, F., Mishnaevski, K., and Kurant, E. (2013). Caspase activity is required
723 for engulfment of apoptotic cells. Mol Cell Biol *33*, 3191-3201.
724 Sievers, C., Platt, N., Perry, V.H., Coleman, M.P., and Conforti, L. (2003). Neurites undergoing
725 Wallerian degeneration show an apoptotic-like process with Annexin V positive staining and
726 loss of mitochondrial membrane potential. Neurosci Res *46*, 161-169.
727 Suzuki, J., Umeda, M., Sims, P.J., and Nagata, S. (2010). Calcium-dependent phospholipid
728 scrambling by TMEM16F. Nature *468*, 834-838.
729 Szymczak, A.L., Workman, C.J., Wang, Y., Vignali, K.M., Dilioglou, S., Vanin, E.F., and Vignali, D.A.
730 (2004). Correction of multi-gene deficiency in vivo using a single 'self-cleaving' 2A peptide-
731 based retroviral vector. Nat Biotechnol *22*, 589-594.
732 Tait, J.F., and Gibson, D. (1992). Phospholipid binding of annexin V: effects of calcium and
733 membrane phosphatidylserine content. Arch Biochem Biophys *298*, 187-191.
734 Tao, J., and Rolls, M.M. (2011). Dendrites have a rapid program of injury-induced degeneration
735 that is molecularly distinct from developmental pruning. J Neurosci *31*, 5398-5405.
736 Tung, T.T., Nagaosa, K., Fujita, Y., Kita, A., Mori, H., Okada, R., Nonaka, S., and Nakanishi, Y.
737 (2013). Phosphatidylserine recognition and induction of apoptotic cell clearance by Drosophila
738 engulfment receptor Draper. J Biochem *153*, 483-491.
739 Wang, X., Li, W., Zhao, D., Liu, B., Shi, Y., Chen, B., Yang, H., Guo, P., Geng, X., Shang, Z*., et al.*
740 (2010). Caenorhabditis elegans transthyretin-like protein TTR-52 mediates recognition of
741 apoptotic cells by the CED-1 phagocyte receptor. Nat Cell Biol *12*, 655-664.
742 Wang, Y., Cella, M., Mallinson, K., Ulrich, J.D., Young, K.L., Robinette, M.L., Gilfillan, S., Krishnan,
743 G.M., Sudhakar, S., Zinselmeyer, B.H*., et al.* (2015). TREM2 lipid sensing sustains the microglial
744 response in an Alzheimer's disease model. Cell *160*, 1061-1071.
745 Wehman, A.M., Poggioli, C., Schweinsberg, P., Grant, B.D., and Nance, J. (2011). The P4-ATPase
746 TAT-5 inhibits the budding of extracellular vesicles in C. elegans embryos. Curr Biol *21*, 1951-
747 1959.

748 Williams, D.W., Kondo, S., Krzyzanowska, A., Hiromi, Y., and Truman, J.W. (2006). Local caspase
749 activity directs engulfment of dendrites during pruning. Nat Neurosci *9*, 1234-1236.
750 Williams, D.W., and Truman, J.W. (2005a). Cellular mechanisms of dendrite pruning in
751 Drosophila: insights from in vivo time-lapse of remodeling dendritic arborizing sensory neurons.
752 Development *132*, 3631-3642.
753 Williams, D.W., and Truman, J.W. (2005b). Remodeling dendrites during insect metamorphosis.
754 J Neurobiol *64*, 24-33.
755 Williamson, A.P., and Vale, R.D. (2018). Spatial control of Draper receptor signaling initiates
756 apoptotic cell engulfment. J Cell Biol *217*, 3977-3992.
757 Wu, H.H., Bellmunt, E., Scheib, J.L., Venegas, V., Burkert, C., Reichardt, L.F., Zhou, Z., Farinas, I.,
758 and Carter, B.D. (2009). Glial precursors clear sensory neuron corpses during development via
759 Jedi-1, an engulfment receptor. Nat Neurosci *12*, 1534-1541.
760 Yan, D., Wu, Y., Feng, Y., Lin, S.C., and Lin, X. (2009). The core protein of glypican Dally-like
761 determines its biphasic activity in wingless morphogen signaling. Dev Cell *17*, 470-481.
762 Yang, H., Chen, Y.Z., Zhang, Y., Wang, X., Zhao, X., Godfroy, J.I., 3rd, Liang, Q., Zhang, M., Zhang,
763 T., Yuan, Q.*, et al.* (2015). A lysine-rich motif in the phosphatidylserine receptor PSR-1 mediates
764 recognition and removal of apoptotic cells. Nat Commun *6*, 5717.
765 Yu, D., Baird, M.A., Allen, J.R., Howe, E.S., Klassen, M.P., Reade, A., Makhijani, K., Song, Y., Liu,
766 S., Murthy, Z.*, et al.* (2015). A naturally monomeric infrared fluorescent protein for protein
767 labeling in vivo. Nat Methods *12*, 763-765.
768 Zhai, R.G., Rizzi, M., and Garavaglia, S. (2009). Nicotinamide/nicotinic acid mononucleotide
769 adenylyltransferase, new insights into an ancient enzyme. Cell Mol Life Sci *66*, 2805-2818.
770 Zhu, X., Libby, R.T., de Vries, W.N., Smith, R.S., Wright, D.L., Bronson, R.T., Seburn, K.L., and
771 John, S.W. (2012). Mutations in a P-type ATPase gene cause axonal degeneration. PLoS Genet *8*,
772 e1002853.
773

774 **MOVIE LEGENDS**

775 **Movie S1**: OrionB-GFP labels degenerating dendrites after injury, related to Figure 3. Time-
776 lapse movie of laser-injured ddaC dendrites from 2.5 to 11 hrs AI, showing OrionB-GFP labeling

777 on injured dendrites. The dendrite arbor on the bottom right was injured while the ones at the top
778 were not. The mobile cells in the OrionB-GFP channel are hemocytes. Time stamp is relative to
779 the first frame.

780 **Movie S2**: AV-mCard labels injured dendrites before dendrite fragmentation, related to
781 Figure 3. Time-lapse movie of laser-injured ddaC dendrites from 2.5 to 5 hrs AI, showing AV-
782 mCard labeling on injured dendrites as early as 2 hrs before fragmentation. The AV-mCard
783 signals that do not colocalize with tdTom signals indicate AV-mCard labeling on injured
784 dendrites of other types of neurons. Time stamp is relative to the frame of dendrite
785 fragmentation.

786 **Movie S3**: AV-mCard fails to label injured dendrites when OrionB-GFP is co-expressed, related
787 to Figure 3. Time-lapse movie of laser-injured ddaC dendrites from 1 to 3 hrs AI showing
788 OrionB-GFP labeling but not AV-mCard labeling on injured dendrites before fragmentation.
789 Time stamp is relative to the frame of dendrite fragmentation.

Supplementary Materials and Methods

Molecular cloning and transgenic flies

orion-mNG2$_{11x4}$-V5-T2A-LexA: Two copies of a gRNA spacer sequence targeting *orion* C-terminus and 3'UTR (Table S2) were cloned into pAC-CR7T-gRNA2.1-nlsBFP (Addgene 170515) according to published protocols (Koreman et al., 2021). The resulting plasmid was digested by PstI and NheI and assembled with four DNA fragments (through NEBuilder HiFi DNA assembly, New England Biolabs, Inc) to make an *orion* gRNA-donor vector. The four DNA fragments include a T2A-LexA-VP16 fragment that was PCR-amplified from pUC57-50-GS-FRTGFP2ALexAVP16-50 (Chen et al., 2014) (a gift from Larry Zipursky), an mNG2$_{11x4}$-V5 DNA fragment (synthesized by Integrated DNA Technologies, Inc.), and 5' and 3' homology arms (surrounding the stop codon of *orion*, ~1 kb each) that were PCR-amplified from the genomic DNA of *w^{1118}*.

UAS-orionA-GFP: OrionA coding sequence (CDS) was PCR-amplified from cDNA clone LD24308 (*Drosophila* Genomics Resource Center) and assembled with a superfolder GFP (sfGFP) fragment into pIHEU-MCS (Addgene 58375) (Sapar et al., 2018), resulting in pIHEU-orionA-GFP.

UAS-orionB-GFP: The first two exons of *orionB*, together with the first intron, was PCR-amplified from *w^{1118}* genomic DNA. The common CDS of OrionA and OrionB was PCR-amplified from LD24308. Both fragments were assembled into pIHEU-orionA-GFP to replace the orionA CDS, resulting in pIHEU-orionB-GFP.

UAS-orionB-CD2-mIFP: A pACU-CD2-mIFP plasmid was first constructed in pACU (Addgene 58373) (Han et al., 2011). The CDS of CD2-mIFP contains, from the N-terminus to the C-terminus, the rat CD2 CDS (AA24 to AA344), mIFP CDS (Yu et al., 2015), and Kir2.1 ER exit signal (Han et al., 2011). The OrionB CDS was then inserted before CD2 to make pACU-orionB-CD2-mIFP.

UAS-orionB^{AX3C}-GFP: An OrionB^{AX3C} coding fragment was amplified from pENTR-orionB-AX$_3$C (Boulanger et al., 2021) and used to replace OrionB in pIHEU-orionB-GFP, resulting in pIHEU-orionB-AX$_3$C-GFP.

UAS-orionB^{AAY}-GFP: The RRY motif in OrionB coding sequence was changed into AAY by mutagenesis PCR. The mutated OrionB fragment was used to replace OrionB in pIHEU-orionB-GFP, resulting in pIHEU-orionB-AAY-GFP.

UAS-orionB^{1}-GFP: A G611D mutation was introduced into OrionB sequence by overlap-extension PCR. The mutated OrionB fragment was used to replace OrionB in pIHEU-orionB-GFP, resulting in pIHEU-orionB-G611D-GFP.

LexAop-orionB-GFP: The OrionB-sfGFP CDS was inserted into KpnI/XbaI sites of pAPLO vector (Poe et al., 2017).

UAS-Drpr$^{\Delta Cyto}$: The extracellular domain and transmembrane domain of Drpr (AA1 to AA827) was PCR-amplified from *UAS-drpr-I* (Logan et al., 2012) genomic DNA. An smFP-HA (non-fluorescent) fragment was PCR-amplified from pCAG-smFP-HA (Viswanathan et al., 2015) (a gift from Loren Looger). The two fragments were cloned into pACU through restriction cloning, resulting in pACU-DrprTM_smGFP(dark).

UAS-smNG2$_{1-10}$: An mNG2$_{1-10}$ fragment was synthesized (Integrated DNA Technologies, Inc.) and cloned into NheI/XbaI-digested pIHEU-sfGFPLactC1C2 (Sapar et al., 2018), resulting in pIHEU-smNG2(1-10).

UAS-CDC50-T2A-ATP8A(E): The CDS of ATP8A isoform E (ATP8A(E)) was PCR-amplified from cDNA clone GH28327 (*Drosophila* Genomics Resource Center) and cloned into EcoRI/XbaI sites of pACU. The ATP8A(E) sequence is preceded by PacI and NheI sites and followed by a FLAG tag and a Kir2.1 ER exit signal (Sapar et al., 2018). In parallel, the CDC50 CDS was PCR-amplified from NB40 cDNA library (Brown and Kafatos, 1988) (a gift from Xinhua Lin) and cloned into EcoRI/XbaI sites of pACU. The CDC50 sequence is preceded by a PacI site and followed by BglII and NheI sites. A T2A fragment generated by annealed oligos was then inserted into the BglII/NheI sites. The CDC50-T2A (PacI/NheI) fragment was then released and cloned into PacI/NheI sites before ATP8A(E), resulting in pACU-CDC50-T2A-ATP8A(E).

drpr-GFP: The sfGFP CDS was inserted seamlessly before the stop codon of Drpr-PE in BAC clone CH321-16B09 according to published protocols of recombineering (Warming et al., 2005). Briefly, the *galK* CDS was first inserted before the stop codon of Drpr-PE in CH321-16B09 in bacterial strain SW102 through *galK*-mediated positive selection. The sfGFP CDS was then used to replace *galK* CDS in SW102 through *galK*-mediated negative selection. The resulting construct was transferred to bacterial strain EPI300 for propagation.

drpr-mNG: A *drpr-mNG* KI donor vector was constructed by assembling a pBluescript backbone and four DNA fragments. The four DNA fragments include the mNG CDS (Shaner et al., 2013), a 3xP3-GFP selection marker modified from pHD-DsRed (Addgene #51434), and 5' and 3' homology arms (surrounding the stop codon of Drpr-PE, ~1 kb each) that were PCR-amplified from CH321-16B09. A dual gRNA expression vector was constructed in pCFD4-U6.1_U6.3 (Port et al., 2014) to target the C-terminus and 3' UTR of *drpr* (Table S2).

gRNA-orion and *gRNA-orion-drpr*: A dual gRNA vector targeting *orion* and a quadruple gRNA vector targeting both *orion* and *drpr* were constructed in pAC-U63-QtgRNA2.1-BR (Addgene 170513) according to published protocols (Koreman et al., 2021).

Transgenic constructs were injected by Rainbow Transgenic Flies to transform flies through φC31 integrase-mediated integration into attP docker sites.

Generation of KI flies

To generate *drpr-mNG*, *drpr* KI donor vector and gRNA-expression vector were co-injected in *Act-Cas9* embryos. Adult flies from injected embryos were crossed to *w1118; TM3/TM6B*. The progeny was screened for green fluorescence in the adult eye. GFP-positive candidates were crossed to y^1 w^{67c23} *Cre(y+)*^{1b}*; D/TM3, Sb*^{1} (BDSC, #851) to remove 3xP3-GFP. GFP-negative candidates were made isogenic and the mNG insertion was confirmed by genomic PCR and sequencing.

To generate *orion-mNG2*$_{11x4}$*-V5-T2A-LexA*, the *orion* gRNA-donor vector was injected into y^1 *nos-Cas9*$^{ZH-2A}$ w^* (BDSC, #54591) embryos. Adult flies from injected embryos were crossed to y^1 w^**; 13XLexAop2-6XGFP*^{attP2}*/TM6B* (BDSC, #52266). GFP-positive female candidates from the progeny were collected to cross with y^1 w^**; TM3/TM6B*. The adult progeny was then screened for GFP-positive males that were white-eyed and RFP-negative (i.e. having no *nos-Cas9*$^{ZH-2A}$). The males were then crossed to FM6 to remove *13XLexAop2-6XGFP*^{attP2} and to

establish isogenic stocks. The -mNG211x4-V5-T2A-LexA insertion is verified by genomic PCR and sequencing.

CRISPR-TRiM

The efficiency of transgenic gRNA lines was validated by the Cas9-LEThAL assay (Poe et al., 2019). Homozygous males of each gRNA line were crossed to *Act-Cas9 w lig4* (BDSC, #58492) homozygous females. *gRNA-orion* crosses yielded viable female progeny and male lethality between 3rd instar larvae to prepupae; *gRNA-drpr* crosses resulted in lethality in late pupae; *gRNA-orion-drpr* crosses yielded viable female progeny and male lethality before wandering 3rd instar larvae. These results suggest that all gRNAs are efficient.

C4da-specific gene knockout was carried out using *ppk-Cas9* (Poe et al., 2019). Tissue-specific knockout in da neuron precursor cells was carried out with *SOP-Cas9* (Poe et al., 2019). Tissue-specific knockout in pan-epidermal cells was carried out using *shot-Cas9* (Ji et al., 2022). Tissue-specific knockout in epidermal cells in the posterior half of each segment was carried out using *hh-Cas9* (Poe et al., 2019). Whole-animal knockout was carried out using *Act-Cas9* (Port et al., 2014).

Live imaging

Animals were reared at 25°C in density-controlled vials (60-100 embryos/vial) on standard yeast-glucose medium (doi:10.1101/pdb.rec10907). Larvae at 96 hours AEL (3rd instar larval stage) or stages specified were mounted in 100% glycerol under coverslips with vacuum grease spacers and imaged using a Leica SP8 microscope equipped with a 40X NA1.30 oil objective. Larvae were lightly anesthetized with isoflurane before mounting. For consistency, we imaged dorsal ddaC neurons from A1-A3 segments (2-3 neurons per animal) on one side of the larvae. Unless stated otherwise, confocal images shown in all figures are maximum intensity projections of z stacks encompassing the epidermal layer and the sensory neurons beneath, which are typically 8–10 μm for 3rd instar larvae.

Injury assay

Injury assay at the larval stage was done as described previously (Sapar et al., 2018). Briefly, larvae at 84 hrs AEL were lightly anesthetized with isoflurane, mounted in a small amount of halocarbon oil under coverslips with grease spacers. The laser ablation was performed on a Zeiss LSM880 Confocal/Multiphoton Upright Microscope, using a 790 nm two-photon laser at primary dendrites of ddaC neurons in A1 and A3 segments. Animals were recovered on grape juice agar plates following lesion for appropriate times before imaging.

Long-term time-lapse imaging

Long-term time-lapse imaging at the larval stage was done as described previously (Ji et al., 2022; Sapar et al., 2018). Briefly, a layer of double-sided tape was placed on the coverslip to define the position of PDMS blocks. A small amount of UV glue was added to the groove of PDMS and to the coverslip. Anesthetized larvae were placed on top of the UV glue on the coverslip and then covered by PDMS blocks with the groove side contacting the larva. Glue was then cured by 365nm UV light. The coverslip with attached PDMS and larvae was mounted on an aluminum slide chamber that contained a piece of moistened Kimwipes (Kimtech Science) paper. Time-lapse imaging was performed on a Leica SP8 confocal equipped with a 40x NA1.3 oil objective and a resonant scanner at digital zoom 0.75 and a 3-min interval. For imaging after

ablation, larvae were pre-mounted in the imaging chamber and subjected to laser injury. The larvae were then imaged 1-2 hours after ablation.

Pinching assay

Larvae at 96 hrs AEL were lightly anesthetized with isoflurane. Gentle pinching was performed at A2 or A3 segment and near the dorsal midline of larvae using a pair of forceps (DUMONT # 3, Fisher Scientifics) without cracking the cuticle. The pinched larvae were imaged after a 2-hr recovery.

Immunohistochemistry

Immunostaining of *Drosophila* larvae was performed as previously described (Poe et al., 2017). Briefly, 3rd instar larvae were dissected in cold PBS, fixed in 4% formaldehyde/PBS for 20 min at room temperature, and stained with the proper primary antibodies (Table S1) for 2 hrs at room temperature and subsequent secondary antibodies (Table S1) for 2 hrs at room temperature.

Image analysis and quantification

Image processing and analyses were done in Fiji/ImageJ or ilastik. For injured dendrites and pruned dendrites marked by *ppk-MApHS*, the pHluorin-positive pixel area in a region of interest (ROI) (ApH), tdTom positive pixel area in the ROI (Atom) were measured and the unengulfment ratio was calculated based on following formula: 100·ApH/Atom. Methods for tracing and measuring C4da neuron dendrite length have been previously described (Poe et al., 2017). Briefly, the images were segmented by Auto Local Threshold and reduced to single pixel skeletons before measurement of skeleton length by pixel distance. The dendrite debris measurement has been described previously (Sapar et al., 2018). Briefly, a region of interest (ROI) was generated by including a quadrant of a neuron's territory. Dendrite debris within the ROI was converted to binary masks based on fixed thresholds. Different thresholds were used for *ppk-C4-tdTom* and *ppk-Gal4 UAS-CD-tdTom* as they have different brightness. The debris pixel area (Adeb), and ROI area (AROI) were measured, and dendrite coverage ratio was calculated based on following formula: 100·ADeb/AROI. For measuring debris dispersion of injured dendrites, dendrite debris was segmented by Auto Threshold (the "Default" method) in a rectangular ROI that was previously covered by injured dendrites. The ROI was divided into 15X15-pixel squares. The debris spread index was the area ratio of all squares containing dendrite debris in the ROI. For measuring Orion-GFP and AV-mCard on dendrites, tdTom signals on dendrites were used to generate dendrite masks for measurement of GFP or mCard mean intensities within the masks. For measuring Drpr-GFP recruitment, tdTom signals on dendrites were used to generate dendrite masks to measure total dendrite area (Atot) and GFP-positive area (AGFP). The Drpr recruitment index was calculated based on the formula: AGFP/Atot. For V5 staining, Drpr staining and Orion-GFP binding on epidermal cells, signals on cell boundaries of epidermal cells were measured. For Orion-GFP variant intensities in hemolymph, the signal in a single optical section was measured. For Orion-GFP variant intensities in fat body, maximum projected image was measured.

Statistical Analysis

R was used to conduct statistical analyses and generate graphs. (*$p < 0.05$, **$p < 0.01$, and ***$p < 0.001$). Statistical significance was set at $p < 0.05$. Data acquisition and quantification were performed non-blinded. Acquisition was performed in ImageJ. Statistical analyses were performed using R. We used the following R packages: car, stats, multcomp for statistical

analysis and ggplot2 for generating graphs. For the statistical analysis we ran the following tests, ANOVA (followed by Tukey's HSD) when dependent variable was normally distributed and there was approximately equal variance across groups. When dependent variable was not normally distributed and variance was not equal across groups, we used Kruskal-Wallis (followed by Dunn's test, p-values adjusted with Benjamini-Hochberg method) to test the null hypothesis that assumes that the samples (groups) are from identical populations. We used Welch's t-test for comparison between two groups. To check whether the data fit a normal distribution, we generated qqPlots to analyze whether the residuals of the linear regression model are normally distributed. We used the Levene's test to check for equal variance within groups. The quantification of percentages of injured dendrites showing different timings of AV binding was compared using Fisher's exact test.

Replication

For all larval and adult imaging experiments, at least 3 biological replications were performed for each genotype and/or condition.

Table S1. Key Resource Table

REAGENT or RESOURCE	SOURCE	IDENTIFIER	ADDITIONAL INFORMATION
Experimental Models: Organisms/Strains			
orion^{1}	(Boulanger et al., 2021)		
orion$^{\Delta C}$	(Boulanger et al., 2021)		
orion$^{\Delta A}$	(Boulanger et al., 2021)		
orion$^{\Delta B}$	(Boulanger et al., 2021)		
orion-mNG2$_{11x4}$*-V5-T2A-LexA (orion*^{KI}*)*	this study		*orion-mNG(11x4)-F2A-LexA::VP16*$^{7A-1}$
Act5C-Cas9	Bloomington Drosophila Stock Center	RRID:BDSC _54590	*Act5C-Cas9.P*
ppk-MApHS	(Han et al., 2014)		*ppk-MApHS*^{1}
UAS-TMEM16F	(Sapar et al., 2018)		*UAS-TMEM16F(D430G)*^{VK00016}
ppk-Gal4	(Han et al., 2012)		*ppk-Gal4*^{VK00037}
21-7-Gal4	(Song et al., 2007)		*GawB*$^{21-7}$
Dcg-Gal4	(Suh et al., 2006)		
UAS-AnnexinV-mCard	(Sapar et al., 2018)		*UAS-AnnexinV-mCard*^{VK00037}
UAS-CD4-tdTom	(Han et al., 2011)		*UAS-CD4-tdTom*^{7M1}
UAS-OrionB-GFP	this study		*UAS-orion(B)-sfGFP*^{VK00018}
UAS-OrionB-Myc	(Boulanger et al., 2021)		*UAS-orion-B-myc*

UAS-CDC50-T2A-ATP8A(E)	this study		*UAS-CDC50-T2A-ATP8A(E)*^{VK00016}
LexAop-OrionB-GFP	this study		*LexAop-orion(B)-sfGFP*^{VK37}
ppk-Cas9	(Poe et al., 2019)		*ppk-Cas9*^{7D}
UAS-Drpr	Bloomington Drosophila Stock Center	RRID:BDSC_67035	*UAS-drpr[I]*
drpr-GFP	this study		*drpr-sfGFP*^{VK00037}
Dcg-LexA	this study		
UAS-Drpr^{Cyto}	this study		*UAS-drprTM-smGFP.HA*^{VK00018}
UAS-OrionB-CD2-mIFP	this study		*UAS-Orion(B)-CD2-mIFP*^{VK00019}
UAS-ATP8A	(Ji et al., 2022)		*UAS-ATP8Acore*^{VK00016}
UAS-OrionB^{AX3C}*-GFP*	this study		*UAS-orion(B.CX3Cmut)-sfGFP*^{VK00018}
UAS-OrionB^{AAY}*-GFP*	this study		*UAS-orion(B.RRYmut)-sfGFP*^{VK00018}
UAS-OrionB^{1}*-GFP*	this study		*UAS-orion(B.G611D)-sfGFP*^{VK00018}
UAS-AVmut-GFP	(Sapar et al., 2018)		*UAS-AnnexinV(mut)-GFP*^{VK00018}
ppk-Cas9	(Poe et al., 2019)		*ppk-Cas9*^{7D}
gRNA-CDC50	(Sapar et al., 2018)		*gRNA-CDC50*^{attP2}
gRNA-Nmnat	(Ji et al., 2022)		*gRNA-NmnatVK00027*
LexAop-GFPnls	Bloomington Drosophila Stock Center	RRID:BDSC _29955	*lexAop-2xhrGFP.nls*^{3a}
gRNA-orion	this study		*gRNA-orion(BR)*^{VK00027}
shot-Cas9	(Ji et al., 2022)		*shot-Cas9*^{1A}
SOP-Cas9	(Poe et al., 2019)		*[sc-E1]x8-Cas9*^{3A}
R16D01-Gal4	Bloomington Drosophila Stock Center	RRID: BDSC_48722	*R16D01-Gal4*^{attP2}
UAS-smNG$_{1-10}$	this study		*UAS-smNG2(1-10)*^{VK00027}
ppk-LexA	(Poe et al., 2017)		*ppk-LexA.GAD*^{3}
LexAop-Wld^{S}	(Ji et al., 2022)		*LexAop-WldS*^{VK00027}
ppk-CD4-tdTom	(Han et al., 2011)		*ppk-spGFP11-CD4-tdTom*^{2}
R16A03-LexA	(Sapar et al., 2018)		*R16A03-LexAp65*^{VK00027}

UAS-mIFP-T2A-HO1	(Poe et al., 2017)	RRID: BDSC_64181	*UAS-mIFP-T2A-HO1*^{VK00005}
UAS-GFP-LactC1C2	(Sapar et al., 2018)		*UAS-GFP-LactC1C2*^{VK00018}
drpr^{-}	(Sapar et al., 2018)		*drpr*^{indel3}
gRNA-drpr	(Ji et al., 2022)		*gRNA-drpr(BR)*^{VK00027}
gRNA-orion-drpr	this study		*gRNA-orion-drpr(BR)*^{VK00027}
hh-Cas9	(Poe et al., 2019)		*R28E04-Cas9*^{6A}
drpr-mNG	this study		*drpr-mNeonGreen*$^{1008-15}$
UAS-Drpr	(Logan et al., 2012)		*UAS-drpr[I]:HA*
R38F11-Gal4	Bloomington Drosophila Stock Center	RRID: BDSC_50014	*R38F11-Gal4*^{attP2}
gRNA-ATP8A	(Sapar et al., 2018)		*gRNA-ATP8A*^{VK00019}
hh-Gal4	(Han et al., 2004)		
Dp(1:3)DC496	Bloomington Drosophila Stock Center	RRID:BDSC_33489	*PBac{DC496}*^{VK00033}
ppk-Gal4	(Han et al., 2012)		*ppk-Gal4*^{1a}
UAS-CD4-tdTom	(Han et al., 2011)		*UAS-CD4-tdTom*^{VK00033}
y^{1} *w*^{67c23} *Cre(y+)*^{1b}*; D/TM3, Sb*^{1}	Bloomington Drosophila Stock Center	RRID:BDSC_851	
y^{1} *nos-Cas9*$^{ZH-2A}$ *w**	Bloomington Drosophila Stock Center	RRID:BDSC_54591	
13XLexAop2-6XGFP	Bloomington Drosophila Stock Center	RRID:BDSC_52266	*13XLexAop2-6XGFP*^{attP2}
Act-Cas9 w lig4	Bloomington Drosophila Stock Center	RRID:BDSC_58492	*y*^{1} *Act5C-Cas9(RFP-)*$^{ZH-2A}$ *w*^{1118} *DNAlig4*^{169}
Recombinant DNA			
pAC-CR7T-gRNA2.1-nlsBFP	(Koreman et al., 2021)	RRID:Addgene_170515	
pUC57-50-GS-FRTGFP2ALexAVP16-50	(Chen et al., 2014)		
LD24308	*Drosophila* Genomics Resource Center		
pIHEU-MCS	(Sapar et al., 2018)	RRID:Addgene_58375	
pACU	(Han et al., 2011)	RRID:Addgene_58373	
pENTR-orionB-AX3C	(Boulanger et al., 2021)		
pAPLO	(Poe et al., 2017)	RRID:Addgene_112805	

pCAG-smFP-HA	(Viswanathan et al., 2015)	RRID:Addgene_59759	
GH28327	*Drosophila* Genomics Resource Center		
NB40 cDNA library	(Brown and Kafatos, 1988)		
CH321-16B09	BACPAC Resources Center		
pGalK	(Warming et al., 2005)		
pHD-DsRed	Addgene	RRID:Addgene_51434	
pCFD4-U6.1_U6.3	(Port et al., 2014)	RRID:Addgene_49411	
pAC-U63-QtgRNA2.1-BR	(Koreman et al., 2021)	RRID:Addgene_170513	
Bacterial Strains			
SW102	(Warming et al., 2005)		
EPI300	Lucigen Corporation	Cat. # C300C105	
Antibody			
Rat-Elav-7E8A10 (1:20)	Developmental Studies Hybridoma Bank	AB_528218	
8D12 anti-Repo (1:20)	Developmental Studies Hybridoma Bank	AB_528448	
V5 Tag Antibody (R960-25) (1:400)	Thermo Fisher Scientific	AB_2556564	
Rabbit anti Drpr polyclonal (1:100)	(Freeman et al., 2003)		
Cy™5 AffiniPure Donkey Anti-Rat IgG (H+L) (1:200)	Jackson ImmunoResearch Labs	AB_2340671	712-175-150
Alexa Fluor® 647 AffiniPure Donkey Anti-Mouse IgG (H+L) (1:200)	Jackson ImmunoResearch Labs	RRID: AB_2340862	715-605-150
Alexa Fluor® 488 AffiniPure Donkey Anti-Rabbit IgG (H+L) (1:200)	Jackson ImmunoResearch Labs	RRID: AB_2313584	711-545-152
Alexa Fluor® 488 AffiniPure Donkey Anti-Mouse IgG (H+L) (1:400)	Jackson ImmunoResearch Labs	RRID: AB_2340846	715-545-150
Software and Algorithms			
Fiji	https://fiji.sc/	RRID: SCR_002285	
R	https://www.r-project.org/	RRID: SCR_001905	

Adobe Photoshop	Adobe	RRID:SCR_014199	
Adobe Illustrator	Adobe	RRID:SCR_010279	
ilastik	(Berg et al., 2019)		
AlphaFold2.ipynb	(Mirdita et al., 2021)		
UCSF Chimera	(Pettersen et al., 2004)		
Other			
NEBuilder® HiFi DNA Assembly Master Mix	New England Biolabs Inc.	#E2621	

Table S2. gRNA target sequences.

Gene	Target sequence 1	Target sequence 2
orion (for KO)	GAAGGGCAACTACACCCAGG	CATGTTTCGTCGGATCACAG
orion (for KI)	GATTCTAAAGCGGAGAGAAG	
drpr (for KO)	CCATGCCGTAGAATCCAGGT	ACGGACAAGGATGCGCCCAG
drpr (for KI)	AGAAATTTCGGACTGGAACT	GCCGGAACAGTCACTTCACC

Reference

Berg, S., Kutra, D., Kroeger, T., Straehle, C.N., Kausler, B.X., Haubold, C., Schiegg, M., Ales, J., Beier, T., Rudy, M., *et al.* (2019). ilastik: interactive machine learning for (bio)image analysis. Nat Methods *16*, 1226-1232.

Boulanger, A., Thinat, C., Zuchner, S., Fradkin, L.G., Lortat-Jacob, H., and Dura, J.M. (2021). Axonal chemokine-like Orion induces astrocyte infiltration and engulfment during mushroom body neuronal remodeling. Nat Commun *12*, 1849.

Brown, N.H., and Kafatos, F.C. (1988). Functional cDNA libraries from Drosophila embryos. J Mol Biol *203*, 425-437.

Chen, Y., Akin, O., Nern, A., Tsui, C.Y., Pecot, M.Y., and Zipursky, S.L. (2014). Cell-type-specific labeling of synapses in vivo through synaptic tagging with recombination. Neuron *81*, 280-293.

Freeman, M.R., Delrow, J., Kim, J., Johnson, E., and Doe, C.Q. (2003). Unwrapping glial biology: Gcm target genes regulating glial development, diversification, and function. Neuron *38*, 567-580.

Frost, J.L., and Schafer, D.P. (2016). Microglia: Architects of the Developing Nervous System. Trends Cell Biol *26*, 587-597.

Han, C., Belenkaya, T.Y., Wang, B., and Lin, X. (2004). Drosophila glypicans control the cell-to-cell movement of Hedgehog by a dynamin-independent process. Development *131*, 601-611.

Han, C., Jan, L.Y., and Jan, Y.N. (2011). Enhancer-driven membrane markers for analysis of nonautonomous mechanisms reveal neuron-glia interactions in Drosophila. Proc Natl Acad Sci U S A *108*, 9673-9678.

Han, C., Song, Y., Xiao, H., Wang, D., Franc, N.C., Jan, L.Y., and Jan, Y.N. (2014). Epidermal cells are the primary phagocytes in the fragmentation and clearance of degenerating dendrites in Drosophila. Neuron *81*, 544-560.

Han, C., Wang, D., Soba, P., Zhu, S., Lin, X., Jan, L.Y., and Jan, Y.N. (2012). Integrins regulate repulsion-mediated dendritic patterning of drosophila sensory neurons by restricting dendrites in a 2D space. Neuron *73*, 64-78.

Ji, H., Sapar, M.L., Sarkar, A., Wang, B., and Han, C. (2022). Phagocytosis and self-destruction break down dendrites of Drosophila sensory neurons at distinct steps of Wallerian degeneration. Proceedings of the National Academy of Sciences *119*, e2111818119.

Koreman, G.T., Xu, Y., Hu, Q., Zhang, Z., Allen, S.E., Wolfner, M.F., Wang, B., and Han, C. (2021). Upgraded CRISPR/Cas9 tools for tissue-specific mutagenesis in Drosophila. Proc Natl Acad Sci U S A *118*.

Logan, M.A., Hackett, R., Doherty, J., Sheehan, A., Speese, S.D., and Freeman, M.R. (2012). Negative regulation of glial engulfment activity by Draper terminates glial responses to axon injury. Nat Neurosci *15*, 722-730.

Mirdita, M., Schütze, K., Moriwaki, Y., Heo, L., Ovchinnikov, S., and Steinegger, M. (2021). ColabFold - Making protein folding accessible to all. bioRxiv, 2021.2008.2015.456425.

Pettersen, E.F., Goddard, T.D., Huang, C.C., Couch, G.S., Greenblatt, D.M., Meng, E.C., and Ferrin, T.E. (2004). UCSF Chimera--a visualization system for exploratory research and analysis. J Comput Chem *25*, 1605-1612.

Poe, A.R., Tang, L., Wang, B., Li, Y., Sapar, M.L., and Han, C. (2017). Dendritic space-filling requires a neuronal type-specific extracellular permissive signal in Drosophila. Proc Natl Acad Sci U S A *114*, E8062-E8071.

Poe, A.R., Wang, B., Sapar, M.L., Ji, H., Li, K., Onabajo, T., Fazliyeva, R., Gibbs, M., Qiu, Y., Hu, Y., *et al.* (2019). Robust CRISPR/Cas9-Mediated Tissue-Specific Mutagenesis Reveals Gene Redundancy and Perdurance in Drosophila. Genetics *211*, 459-472.

Port, F., Chen, H.M., Lee, T., and Bullock, S.L. (2014). Optimized CRISPR/Cas tools for efficient germline and somatic genome engineering in Drosophila. Proc Natl Acad Sci U S A *111*, E2967-2976.

Sapar, M.L., Ji, H., Wang, B., Poe, A.R., Dubey, K., Ren, X., Ni, J.Q., and Han, C. (2018). Phosphatidylserine Externalization Results from and Causes Neurite Degeneration in Drosophila. Cell Rep *24*, 2273-2286.

Shaner, N.C., Lambert, G.G., Chammas, A., Ni, Y., Cranfill, P.J., Baird, M.A., Sell, B.R., Allen, J.R., Day, R.N., Israelsson, M., *et al.* (2013). A bright monomeric green fluorescent protein derived from Branchiostoma lanceolatum. Nat Methods *10*, 407-409.

Song, W., Onishi, M., Jan, L.Y., and Jan, Y.N. (2007). Peripheral multidendritic sensory neurons are necessary for rhythmic locomotion behavior in Drosophila larvae. Proc Natl Acad Sci U S A *104*, 5199-5204.

Suh, J.M., Gao, X., McKay, J., McKay, R., Salo, Z., and Graff, J.M. (2006). Hedgehog signaling plays a conserved role in inhibiting fat formation. Cell Metab *3*, 25-34.

Viswanathan, S., Williams, M.E., Bloss, E.B., Stasevich, T.J., Speer, C.M., Nern, A., Pfeiffer, B.D., Hooks, B.M., Li, W.P., English, B.P., *et al.* (2015). High-performance probes for light and electron microscopy. Nat Methods *12*, 568-576.

Warming, S., Costantino, N., Court, D.L., Jenkins, N.A., and Copeland, N.G. (2005). Simple and highly efficient BAC recombineering using galK selection. Nucleic Acids Res *33*, e36.

Yu, D., Baird, M.A., Allen, J.R., Howe, E.S., Klassen, M.P., Reade, A., Makhijani, K., Song, Y., Liu, S., Murthy, Z., *et al.* (2015). A naturally monomeric infrared fluorescent protein for protein labeling in vivo. Nat Methods *12*, 763-765.